aptara | GJI | gji_3910 | Dispatch: July 29, 2008 | CE:
Journal | MSP No. | No. of pages: 22 | PE: Gregor

Geophys. J. Int. (2008) doi: 10.1111/j.1365-246X.2008.03910.x

Interplate coupling and transient slip along the subduction interface beneath Oaxaca, Mexico

F. Correa-Mora,[1] C. DeMets,[1] E. Cabral-Cano,[2] B. Marquez-Azua[3] and O. Diaz-Molina[2]

[1]*Geology and Geophysics, University of Wisconsin-Madison, Madison, WI,* 53706*, USA. E-mail: chuck@geology.wisc.edu*
[2]*Departamento de Geomagnetismo y Exploracion, Instituto de Geofisica, Universidad Nacional Autonoma de Mexico, Ciudad Universitaria, Mexico DF,* 04510*, Mexico*
[3]*DGOT/SisVoc,Universidad de Guadalajara, Av. Maestros y Mariano Barcenas,* 93106*, Guadalajara, Jalisco, Mexico*

Accepted 2008 July 6. Received 2008 July 6; in original form 2008 February 4

SUMMARY

We describe and model GPS measurements of surface deformation from the Oaxaca segment of the Mexican subduction zone to characterize interseismic strain accumulation and episodic transient slip in this region and test seismologically-based models of strain accumulation and release along subduction interfaces. Deformation measured from 2001 to 2007 within our dense 31-station GPS array has consisted of (1) trench-normal horizontal contraction at rates that decrease monotonically inland from the coast, (2) rapid coastal subsidence that changes gradually to slow uplift at locations more than 100 km inland and (3) periods of transient slip that interrupt the otherwise steady deformation. Inverse modelling of transient station offsets in 2004 and 2006 indicates that transient slip along the subduction interface occurred downdip from the rupture limits of previous large earthquakes in this region in both 2004 and 2006. GPS site velocities that are corrected for the effects of this transient slip, vary significantly over distances of only tens of kilometres both along the coastline and inland, implying that similar spatial variations occur in the degree of locking across the subduction interface. Deformation rates measured along the coast reach their maximum above the core of the rupture zone of the 1978 $M_s = 7.8$ shallow-thrust earthquake and generally decrease outwards towards the edges of the rupture zone. Bounded-value, inverse modelling of the interseismic GPS velocity field with a finite element mesh that simulates the study region indicates that much of the rupture zone of the 1978 shallow-thrust earthquake is fully locked at the plate convergence rate, but that this region is surrounded by weakly locked areas of the subduction interface, which may slow or arrest the propagation of future earthquakes. Much of the deeper region of transient slip, downdip from the seismogenic zone, is also fully locked between the episodes of transient slip; however, the elastic energy that accumulated due to locking of this deeper transitional zone between 2002 and 2006 appears to have been mostly or completed released by the 2004 and early 2006 transient slip events. The approximately balanced energy budget for the deeper zone of transient slip implies that this region is unlikely to contribute significant elastic energy to future earthquakes that originate along the seismogenic zone. Our results support a model in which seismic asperities coincide with regions of strong locking between earthquakes. The potential elastic energy that has re-accumulated since 1978 in the seismogenic zone is already sufficient to cause a repeat of the 1978 earthquake.

Key words: Seismic cycle; Transient deformation; Subduction zone processes.

1 INTRODUCTION

The stick-slip model of the subduction earthquake cycle has long been the starting basis for evaluations of fault behaviour and earthquake hazard. Proposed originally to consist of long periods of linear interseismic elastic strain accumulation that culminate in earthquakes (Reid 1910), this simple model has since undergone major modifications in response to both theoretical and observational advances. Over the past two decades, such advances have included the exposition of empirically-based rate- and state-variable friction laws (Scholz 1998) and discoveries of a broad range of previously unknown slow-slip phenomena, such as silent earthquakes

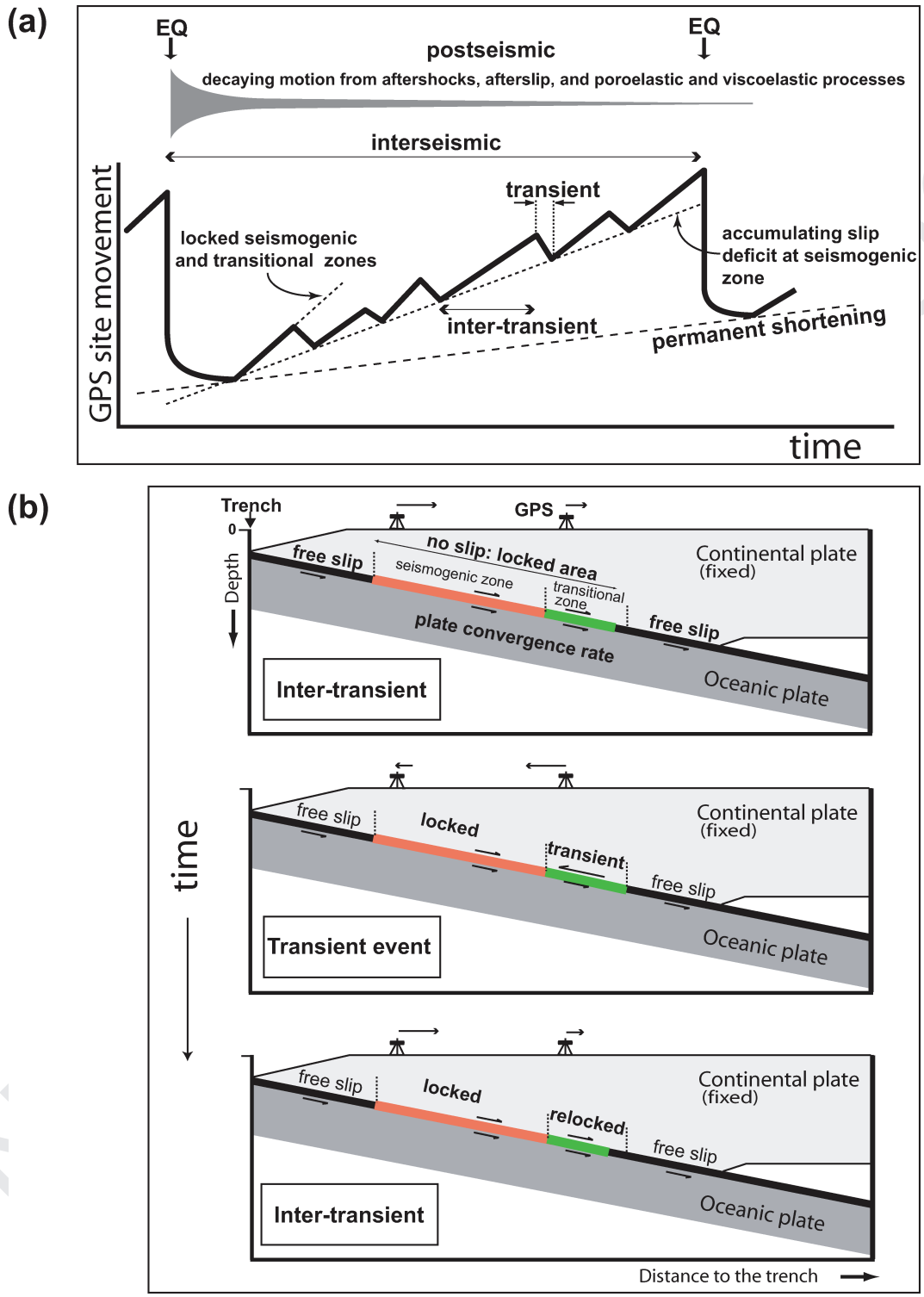

Figure 1. (a) Surface deformation versus time for the model of the seismic cycle shown in (b). (b) Subduction interface behaviour and surface displacements during the interseismic phase of the seismic cycle, including periods of transient slip that are superimposed on interseismic strain accumulation.

COLOUR FIG.

and aseismic transient slip events, which alongwith fault creep may collectively accommodate as much as 70 per cent of plate convergence (Pacheco *et al.* 1993; McCaffrey 1997).

Fig. 1(a) presents a simplified view of a generic subduction earthquake cycle, both in space and time. To first order, strain accumulation and release are characterized by long periods of linear interseismic elastic strain accumulation that are terminated by earthquakes. The earthquakes trigger a variety of postseismic responses that include fault afterslip, representing a delayed frictional response of velocity-strengthening areas of the subduction interface (Marone 1998) viscoelastic flow of the lower crust and upper mantle that relaxes the coseismic stress jump in those regions (Thatcher & Rundle

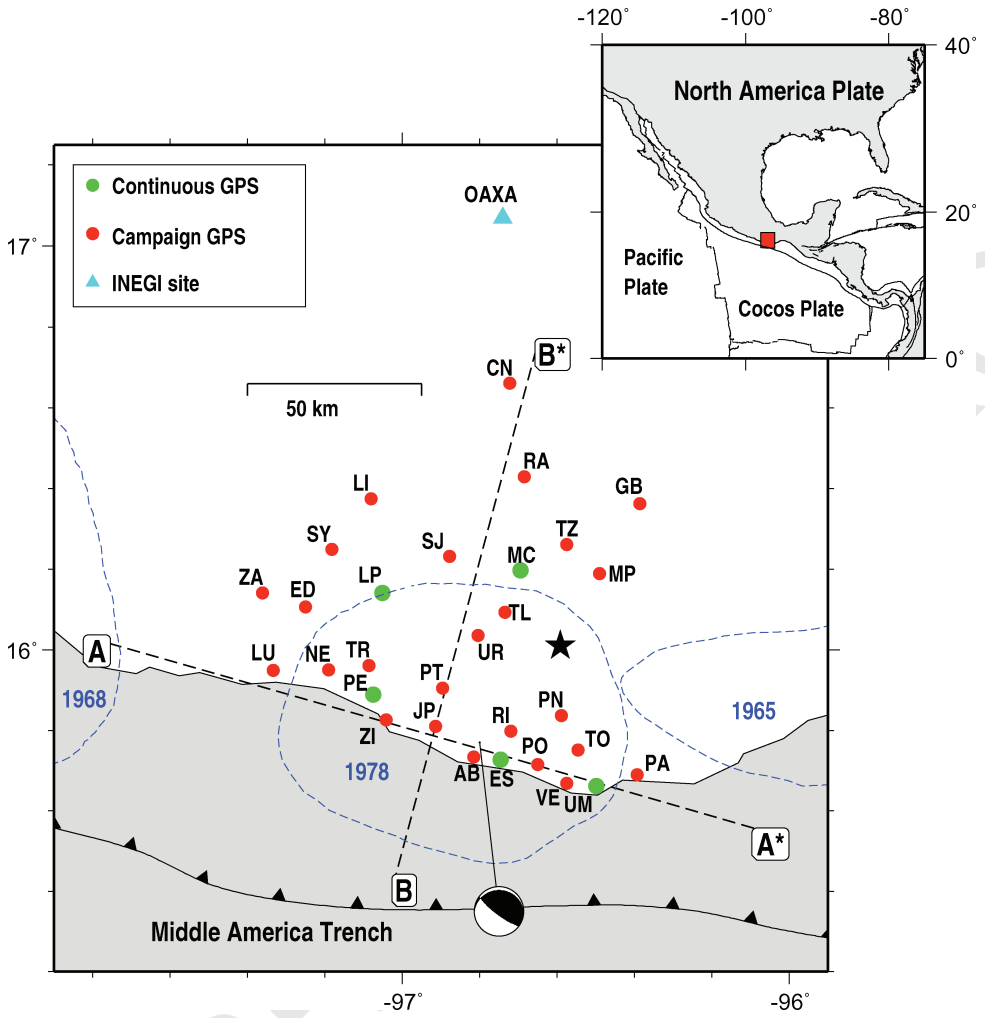

Figure 2. Map of the study area. Green and red circles show continuous and campaign stations in the Oaxaca network, respectively. INEGI GPS station OAXA is shown with a blue triangle. Dashed lines specify the rupture zones of large subduction thrust earthquakes in 1965, 1968 and 1978 (Singh *et al.* 1980; Tajima & McNally 1983). Focal mechanism and epicentre (star) are shown for the M_s 7.8, 1978 Oaxaca earthquake (Singh *et al.* 1980). Profiles A–A* and B–B* are described later in the text. Inset shows the tectonic setting of the study area (red rectangle).

COLOUR FIG.

1984), and poroelastic deformation, representing diffusion-limited flow of fluids in response to coseismic pore-space volume changes (Wang 2000). The deformations that are induced by these postseismic processes obey different decay laws and decay over different timescales. In the absence of interseismic transient slip events, deformation at the surface thus represents a superposition of linear elastic strain accumulation from the frictionally locked areas of the subduction interface and non-linear deformation from postseismic processes. For faults with earthquake recurrence intervals that are significantly longer than the time periods over which postseismic deformation decay, surface deformation will asymptotically approximate linear deformation late, in the earthquake cycle (Fig. 1a).

A further modification to the stick-slip model has been necessitated by widespread discoveries of aseismic transient slip events, including Cascadia (Dragert *et al.* 2001), Japan (Ozawa *et al.* 2002; Obara *et al.* 2004), Mexico (Lowry *et al.* 2001; Kostoglodov *et al.* 2003), New Zealand (Douglas *et al.* 2005) and Alaska (Ohta *et al.* 2006). These transient slip events typically originate downdip from seismogenic zone and release elastic strain that causes sites in the upper plate to move toward the trench, for periods of weeks to months, opposite their normal landward direction of interseismic motion (Fig. 1b). As a consequence, the interseismic phase of the earthquake cycle for faults where transient slip occurs must be subdivided into 'intertransient' periods during which the seismogenic zone and deeper transient slip zone are both locked and contribute to more rapid elastic shortening of the upper plate and periods of transient slip, during which some elastic strain is fully or partly relieved by aseismic slip along the deeper zone.

Here, we extend the effort to better understand how downdip motion of a subducting plate is accommodated in space and time, using finite element modelling of dense GPS station measurements from the state of Oaxaca in southern Mexico (Fig. 2). The seismically active Oaxaca segment of the Middle America trench, which accommodates Cocos–North America plate motion, is well suited for a detailed study of the inter-relationships between intertransient strain accumulation, transient slip and seismic asperities. With average trench-to-coast distances of only 45–55 km, the central Oaxaca segment is one of the few places on Earth where geodetic measurements can be made directly above large areas of the seismogenic region of a subduction interface. Subduction of the Cocos plate at rates of 67–74 mm yr^{-1} (DeMets 2001) and a shallow-dipping subduction interface yield surface deformation rates in the field area

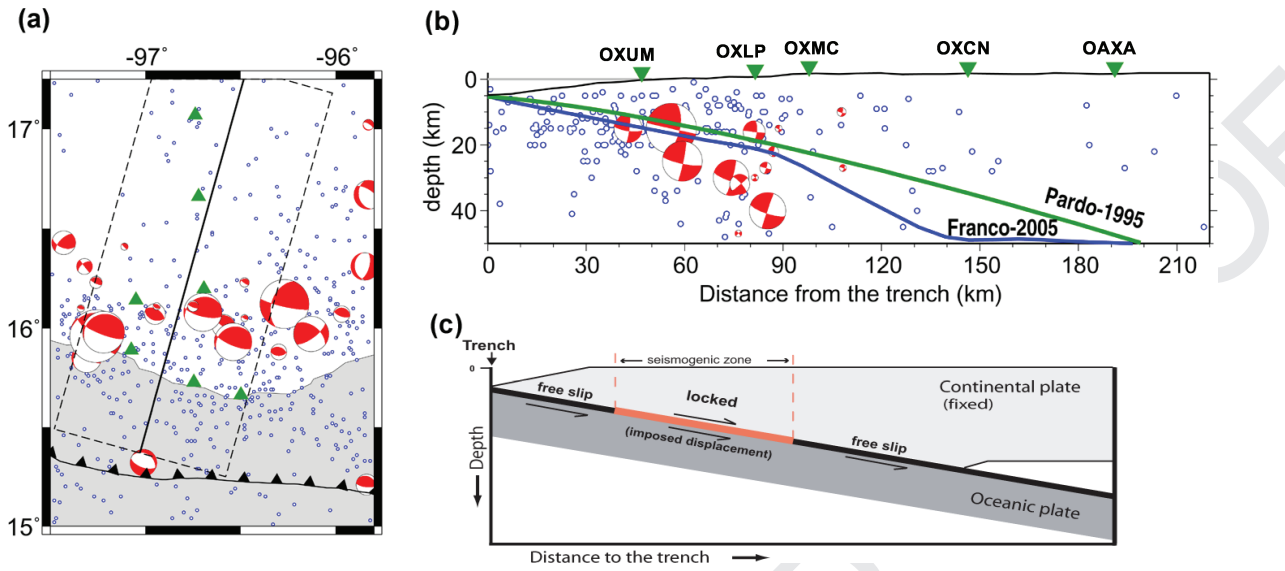

Figure 3. (a) Oaxaca regional seismicity. Hypocentres for earthquakes ($M_W \geq 4$) are from the Mexican Seismological Service (SSN) for the period 1974–2001. Earthquake focal mechanisms are from Stewart *et al.* (1981), Suarez *et al.* (1990) and Harvard centroid moment tensor solutions. Focal mechanisms are scaled by magnitude. Green triangles are GPS stations. Black-solid line indicates location of the profile for the cross-section shown in (b). (b) Depth versus distance cross-section, with model plate interface geometries used in this study. Interfaces that are labelled Pardo-1995 (green) and Franco-2005 (blue) are approximations of the subduction interface from Pardo & Suárez (1995) and Franco *et al.* (2005), respectively. (c) Driving mechanism for interface slip in the FEM. Kinematic constraints that are applied to freely slipping and no-slip areas are described in the text.

that are easily measured with GPS, another key requirement for a study of this type.

An important motivation for our work is its potential for improving our understanding of seismic hazard along the Mexican subduction zone, which endangers large areas of southern and central Mexico, including Mexico City, the national capital and one of the world's most heavily populated urban areas. Along the Oaxaca subduction segment (Figs 2 and 3), large shallow-thrust earthquakes ruptured the subduction interface in 1965 ($M_s \sim 7.6$), 1968 ($M_s \sim 7.1$) and 1978 ($M_s \sim 7.8$) (Stewart *et al.* 1981; Suarez *et al.* 1990), thereby demonstrating its significant seismic potential. In addition, transient slip events in the same region in 2004 and 2006 released elastic energy equivalent to $M_W \approx 7.0$ earthquakes (Lowry 2006; Brudzinski *et al.* 2007), raising obvious questions about whether transient slip might trigger future destructive megathrust earthquakes or possibly relieve some elastic strain at seismogenic levels of the subduction zone and hence reduce the long-term seismic hazard.

2 DATA AND DATA PROCESSING

The GPS data used in this study come from six continuous stations and 25 campaign sites that extend ~110 km along the Pacific coast of Oaxaca and ~125 km inland (Fig. 2 and Table 1). Station OAXA has been recording continuously since early 1993, longer than any other station in the study area and is operated by the Mexican agency 'Instituto Nacional de Estadistica, Geografia e Informatica' (INEGI; Marquez-Azua & DeMets 2003). We installed the other five continuous stations between mid-2001 and mid-2002 to track any temporal variations in surface deformation and also installed and occupied 25 campaign sites, beginning in mid-2001. The average station spacing of 10–20 km was designed to enable the resolution of slip features as small as 20 km on a side along the underlying subduction interface. Nearly all of the 25 campaign sites have been occupied 3–5 times, with a typical station occupation consisting of three 18–24 hr sessions. The continuous and campaign GPS time-series span 1.3 to 5.1 yr, with an average of 4.2 yr.

GPS phase and code measurements are analysed with GIPSY software from the Jet Propulsion Laboratory (JPL). We apply a precise point-positioning analysis strategy (Zumberge *et al.* 1997) and use fiducial-free satellite orbits and satellite clock corrections from JPL. Phase ambiguities are also estimated and removed when possible. Daily station locations are estimated initially in a no-fiducial reference frame (Heflin *et al.* 1992) and are then transformed to ITRF2000 (Altamimi *et al.* 2002), using daily seven-parameter Helmert transformations from JPL. Scatter in the GPS station positions is further reduced by estimating and removing any spatially correlated noise between sites (Marquez-Azua & DeMets 2003). Station velocities are estimated via linear regression of the three geocentric station coordinates (Figs 4 and 5), and velocity uncertainties are determined using an empirically-derived error model that accounts for different noise components in the time-series (Mao *et al.* 1999).

All GPS station motions relative to ITRF2000 are transformed to a reference frame fixed to the North American plate, by using an angular velocity that specifies the motion of the North American plate relative to ITRF2000 at the location of each of our GPS sites. This angular velocity, which we determined from an inversion of the horizontal velocities of several hundred North American plate continuous GPS stations for which we process daily data, yields well-determined estimates of North American plate motion in our study area, with uncertainties of only ± 0.1 mm yr^{-1}. The stations we selected to estimate North American plate motion are limited to sites with time-series longer than 3 yr and exclude stations from areas of significant post-glacial rebound (Calais *et al.* 2006) and the broad deforming zone in the western United States.

Fig. 4 shows the horizontal components of the continuous coordinate time-series in our study area. All of the continuously recording

Table 1. GPS station information and velocities.

Site				North (mm yr^{-1})			East (mm yr^{-1})			Vertical (mm yr^{-1})			Imp.
	Lat °N	Lon °E	Height	V_n	$\pm1\sigma$	Misfit	V_e	$\pm1\sigma$	Misfit	V_v	$\pm1\sigma$	Misfit	per cent
OXPA	15.6899	−96.3929	14.65	18.6	0.6	−0.1	15.2	1.2	0.2	−8.6	2.2	0.6	6.1
OXLU	15.9491	−97.3328	16.81	24.3	2.5	0.1	16.1	3.8	−0.5	−14.4	6.1	−9.8	5.8
OXGB	16.3629	−96.3863	1769.65	14.5	1.9	−0.9	10.5	2.9	−2.0	−6.6	5.0	−3.2	5.6
OXZA	16.1415	−97.3613	831.63	18.3	1.0	0.1	14.9	2.6	1.7	−12.0	4.3	−1.9	5.2
OXCN	16.6605	−96.7218	1558.05	15.2	1.9	−1.3	9.7	2.9	0.7	−0.6	4.7	−3.0	4.8
OXLI	16.3745	−97.0799	947.83	18.8	2.1	−1.4	11.4	3.5	−0.1	−21.0	5.9	−12.2	4.0
OXUM[a]	15.6622	−96.4990	82.17	22.1	0.8	0.7	14.0	0.8	−0.1	−5.7	1.7	1.8	3.8
OAXA[a]	17.0800	−96.7200	1595.86	11.5	0.5	−0.2	7.9	0.8	0.8	4.4	1.0	0.2	3.8
OXSY	16.2488	−97.1821	1755.56	17.4	2.0	−2.8	15.4	3.1	2.2	−19.9	6.2	−8.2	3.6
OXMP	16.1872	−96.4865	2708.70	26.7	6.8	6.1	17.6	12.1	2.8	−2.8	16.8	5.6	3.5
OXZI	15.8266	−97.0421	33.96	32.3	1.8	−0.3	23.2	2.9	1.4	−13.2	4.7	−2.1	3.5
OXAB	15.7340	−96.8152	4.10	33.0	1.7	−0.7	20.5	2.8	2.2	−6.7	7.0	3.8	3.5
OXPN	15.8367	−96.5895	206.12	20.9	2.1	−1.4	16.6	2.8	1.0	−13.8	5.8	−7.3	3.3
OXPT	15.9056	−96.8964	51.41	31.9	1.8	0.7	20.2	2.9	2.4	−18.6	4.7	−4.3	2.9
OXVE	15.6682	−96.5752	7.83	23.3	0.6	−0.4	16.8	2.3	2.1	−12.2	3.4	−4.4	2.9
OXRA	16.4299	−96.6849	1577.05	19.1	2.1	−0.1	10.8	2.8	−2.9	−7.9	4.7	−5.0	2.9
OXED	16.1061	−97.2501	807.32	21.0	1.0	−0.0	13.3	3.2	−1.8	−10.4	4.2	1.8	2.8
OXTO	15.7515	−96.5464	83.50	20.9	1.7	−0.7	15.8	2.6	0.6	−12.1	4.3	−3.5	2.6
OXJP	15.8108	−96.9140	40.56	32.8	1.8	−0.6	23.4	2.6	3.8	−17.8	4.2	−3.8	2.6
OXNE	15.9505	−97.1908	12.89	27.8	1.0	0.8	18.2	2.8	−0.7	−14.1	3.1	−3.6	2.5
OXES	15.7269	−96.7463	4.37	31.7	0.8	0.7	16.0	1.1	−0.9	−9.0	2.0	1.0	2.5
OXTR	15.9608	−97.0857	181.10	28.3	1.9	−0.2	18.7	2.8	−0.5	−14.9	4.3	−0.7	2.4
OXLP[a]	16.1417	−97.0511	835.09	25.5	1.1	−0.1	16.7	2.4	0.9	−12.9	3.0	0.6	2.4
OXRI	15.7981	−96.7194	105.28	27.2	5.3	−1.2	11.4	11.4	−5.0	−13.2	12.8	−2.8	2.3
OXPE[a]	15.8887	−97.0753	75.74	30.1	1.2	−0.5	21.6	1.1	0.8	−14.7	2.1	−2.3	2.3
OXUR	16.0363	−96.8036	821.28	30.6	1.3	0.5	14.1	1.1	−1.5	−12.6	5.2	−4.0	2.3
OXSJ	16.2321	−96.8781	1995.57	24.1	2.1	−2.3	16.5	2.8	1.0	−15.6	5.0	−5.7	2.2
OXTL	16.0938	−96.7348	1513.49	28.8	2.5	−0.2	16.8	3.6	1.1	−11.8	7.1	−4.5	2.2
OXPO	15.7150	−96.6497	9.94	25.4	1.7	−0.9	18.3	2.5	2.6	−13.4	4.3	−4.8	2.2
OXMC[a]	16.1970	−96.6944	1871.46	24.8	1.7	−0.9	16.6	1.3	0.4	−12.1	2.9	−3.6	2.0
OXTZ	16.2608	−96.5755	1752.48	20.4	2.0	−0.8	15.1	3.2	−0.4	−9.6	5.2	−1.7	1.9

Note: Station velocities are specified relative to North American plate and have been corrected for the effects of the 2004 and 2006 transient slip events. Station heights are in metres. Misfits represent the velocity that is predicted by the best-fitting model (see text) subtracted from the observed velocity. Imp. specifies data importance per site, representing the sum of the north, east and vertical importances expressed as a percentage of the sum of all the data importances. Sites are sorted in descending order based on their normalized importance.

[a] Continuous stations.

sites move steadily northeastwards towards the plate interior for periods of months to years, occasionally reverse their sense of motion for periods of weeks to months and then resume steady motion to the northeast. Four episodes of the reverse-sense transient slip occurred between 2001 and 2007. The first, in late 2001, is only weakly expressed in our study area and appears to be associated with a much larger transient slip event from the adjacent state of Guerrero (Kostoglodov *et al.* 2003). The second transient slip episode, which is well recorded at station OAXA in 2002 and appears to have lasted for up to six months, is also expressed in the time-series for station OXUM, possibly as two distinct shorter transients. Little is known about this transient, which was previously identified, but not modelled by Lowry (2006). Better recorded transient slip episodes in early 2004 and early 2006 are described and modelled by Brudzinski *et al.* (2007) and Larson *et al.* (2007). Transient slip events thus occur frequently in our study area and are incorporated in our analysis.

The 25 campaign sites also move landwards (Figs 5 and 6a) at rates that decrease with distance from the coast. Because these sites were measured too infrequently to define the transient slip events that appear in the continuous time-series, we use the continuous time-series to estimate the magnitude and direction of transient offsets (Section 4.1). We then apply a correction to each GPS station time-series for the effects of the transient slip before modelling intertransient strain accumulation (Section 4.2).

3 TECHNIQUES

3.1 Finite element mesh: validation and sensitivity tests

All of our modelling is accomplished using the commercial finite element modelling software ABAQUS (version 6.4.1) and a 3-D finite element mesh that simulates the subduction interface in our study area. The finite element model (FEM) consists of a denser mesh that is centred on the study area (Fig. 7a) and is embedded in a larger regional mesh, whose dimensions are large enough to minimize any edge effects within the study area (Fig. 7b). The node spacings in the dense part of the mesh are 10 km along-strike and 7 km downdip, close to the average GPS station spacing on the surface. The upper surface of the mesh mimics topography and seafloor bathymetry from the 2-minute global compilation of Smith & Sandwell (1997). The mesh is also layered (Fig. 8) to allow for vertical variations in its properties, as described below. During the modelling, the upper surface of the mesh is allowed to deform freely, whereas the lateral and base boundaries of the mesh are pinned.

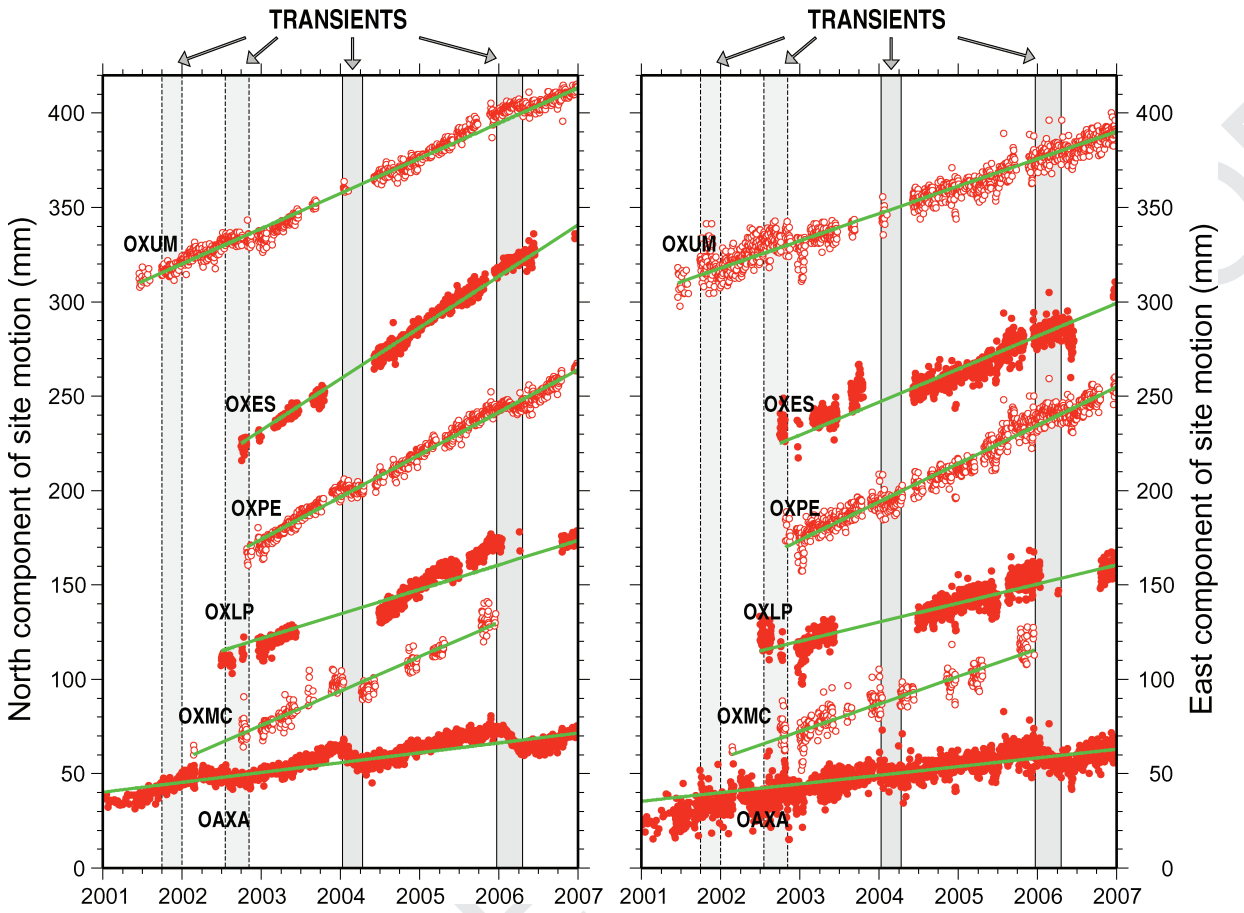

Figure 4. Horizontal components of continuous GPS coordinate time-series used in this study. Site motions are referenced to the North American plate interior. Green line is the best fit velocity for a linear regression of the whole series. Transient slip events are indicated by grey bars (see text for details).

COLOUR FIG.

The rheologies and thicknesses that we assign to the different mesh layers are derived from the CRUST2 model (Bassin *et al.* 2000) (Fig. 8; Table 2), which uses tomographically-defined values of V_P to estimate V_S and density. We extract V_P, V_S and density from CRUST2 for our study area and use them to calculate Poisson's ratio and Young's modulus, which are used to define the elastic properties.

Our study area is located along a section of the trench, where the subduction interface makes a transition from a subhorizontal geometry farther west (Franco *et al.* 2005) to a steeper geometry along the Chiapas segment. We considered two proposed geometries for the subduction interface in our study area (Fig. 3b), one consisting of a smoothly curved geometry constrained by seismological data (Pardo & Suárez 1995) and the other consisting of a subhorizontal geometry that is optimized for the subduction zone ~200 km west of our study area (Franco *et al.* 2005). Since there is no strong *a priori* basis to prefer either geometry for our study area, we embedded the two interfaces in separate 3-D meshes and repeated all of the calculations described below for both geometries. The seismologically based geometry (Pardo & Suárez 1995) yields the best fit to the data, and we thus base the calculations and figures below on results derived using that geometry. We note, however, that none of the principal conclusions described below change significantly if we, instead, employ the subhorizontal subduction interface geometry. In Sections 4.1 and 4.2.4, we discuss the sensitivity of our modelling results to the assumed interface geometry.

Dislocations or, equivalently, slip rates at the node-pairs that define the subduction interface are prescribed kinematically, following Masterlark Masterlark (2003). Forward modelling with the FEM to determine the elastic response at each GPS station for a unit displacement or unit slip rate at each node-pair on the subduction interface is used to determine Green's functions that are the basis for the inverse modelling described in Section 3.3.

We tested the sensitivity of our FEM predictions to the boundary conditions that we impose on the mesh by comparing the deformation that is predicted in the centre of our study area for models in which we enforce different kinematic constraints on the motions of the nodes that define the lateral and bottom boundaries of the extended mesh. The deformation in our study area varies insignificantly as a function of the imposed boundary constraints, thereby indicating that the edges of our extended mesh are far enough from the study area to minimize the effects of the applied boundary constraints.

We also tested the influence of the assumed elastic properties on the predicted deformation, both to validate the FEM and determine whether the layered rheology we use in our FEM (Table 2) yields surface deformation that differs significantly from that predicted by a FEM with homogeneous elastic properties. Extensive testing of our mesh, applying homogeneous elastic properties throughout, yields elastic displacements that agree, to high precision, with analytical homogeneous elastic half-space solutions, thereby validating

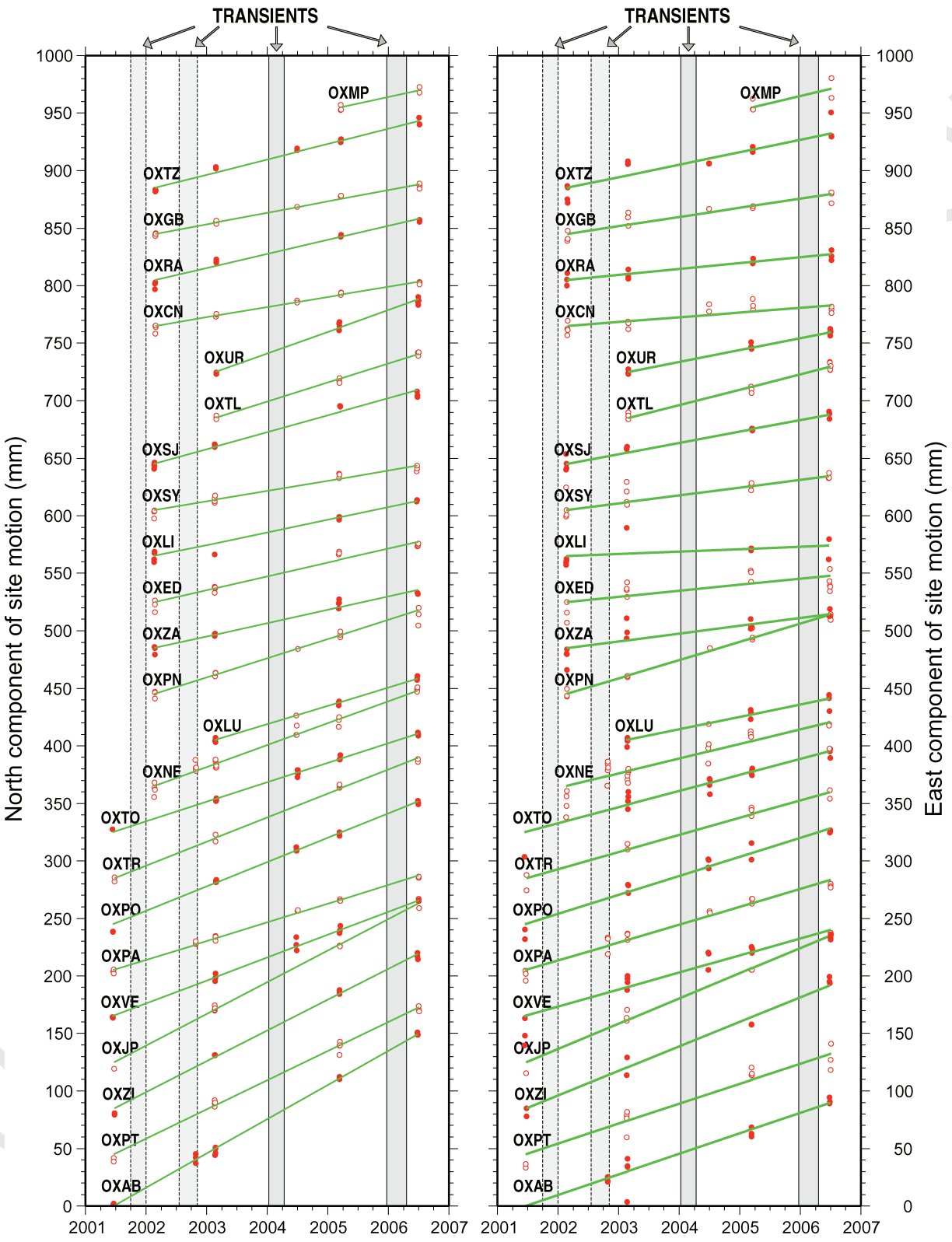

Figure 5. Horizontal components of campaign GPS coordinate time-series used in this study. Site motions are referenced to the North American plate interior. Green line is the best fit velocity for a linear regression of the whole series. Transient slip events are indicated by grey bars (see text for details).

COLOUR FIG.

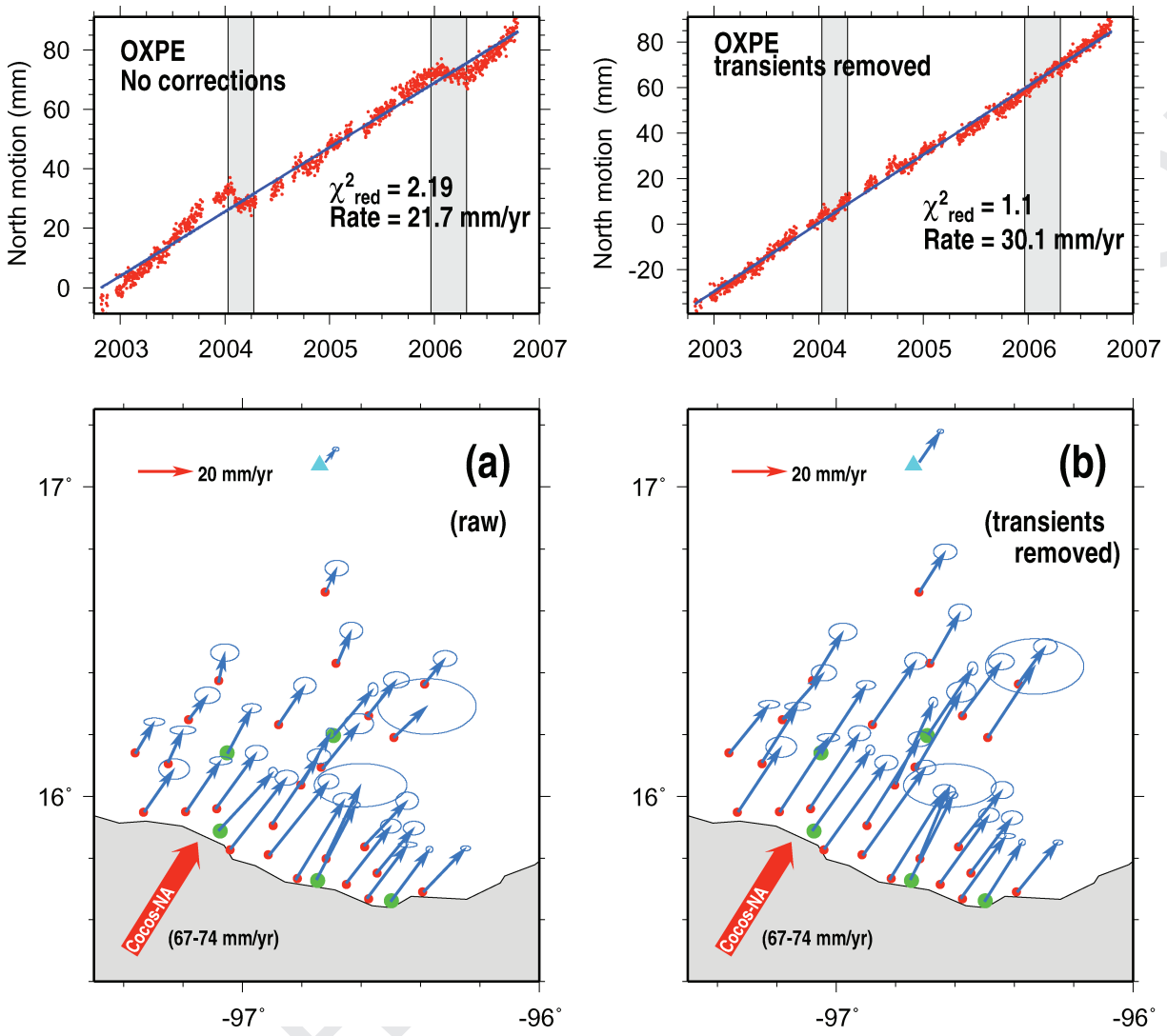

COLOUR FIG.

Figure 6. (a) GPS site velocities relative to North America plate from 2001.5 to 2006.5, without any corrections for transient slip. (b) GPS station velocities, corrected for transient slip, estimated for early 2004 and early 2006. Uncertainty ellipses are 2-D, 1σ. The red arrow indicates the Cocos–North America plate convergence direction and range of rates (in parenthesis) predicted for the study area (DeMets 2001). Upper panel: linear fit to the north component of the GPS time-series for station OXPE before (left-hand side) and after (right-hand side) corrections are applied for transient deformation in 2004 and 2006. Grey bars indicate the transient slip events. The fit, as measured by reduced χ^2, improves by a factor of two and the estimated rate increases by ~40 per cent after correcting the time-series for transient offsets.

the FEM. In contrast, the deformation rates that are predicted by the layered FEM that we employ for our modelling (Fig. 8), differ by several mm yr^{-1} at many of our GPS sites from the deformation rates that are predicted by the homogeneous FEM. These differences are comparable to or larger than the few mm yr^{-1} or smaller uncertainties that are typical of GPS site velocities and are thus large enough to merit the additional complexity of a layered FEM approach. These results reinforce conclusions reached by Masterlark *et al.* (2001) and Zhao *et al.* (2004), who also find significant differences in the deformation predicted by homogeneous and layered FEMs in thrust fault settings.

3.2 Viscoelastic effects

Prior to modelling our GPS observations, we assessed whether the surface deformation from an assumed viscoelastic response of the mantle wedge beneath Oaxaca to the $M_s = 7.8$, 1978 November 29 Oaxaca earthquake is large enough to merit incorporation into our GPS velocity modelling effort. Using the coseismic slip distribution for the 1978 earthquake estimated by Singh *et al.* (1980) and a typical upper-mantle viscosity of 10^{19} Pa s, we extrapolated the time-dependent surface response at decadal intervals from 1978 to 2028, to the viscous relaxation of the coseismic stresses in the upper mantle (Fig. 9). The predicted deformation rates decay rapidly after the earthquake (see inset to Fig. 9) and average 0.1–0.5 mm yr^{-1} at all locations in the study area for the period covered by our measurements (2001–2007). The maximum signal is thus no more than a few per cent of the measured station motions that are described and modelled below, too small to affect any of our results.

3.3 Inverse modelling

The results presented below include multiple inversions of the measured transient offsets and the intertransient station velocities to

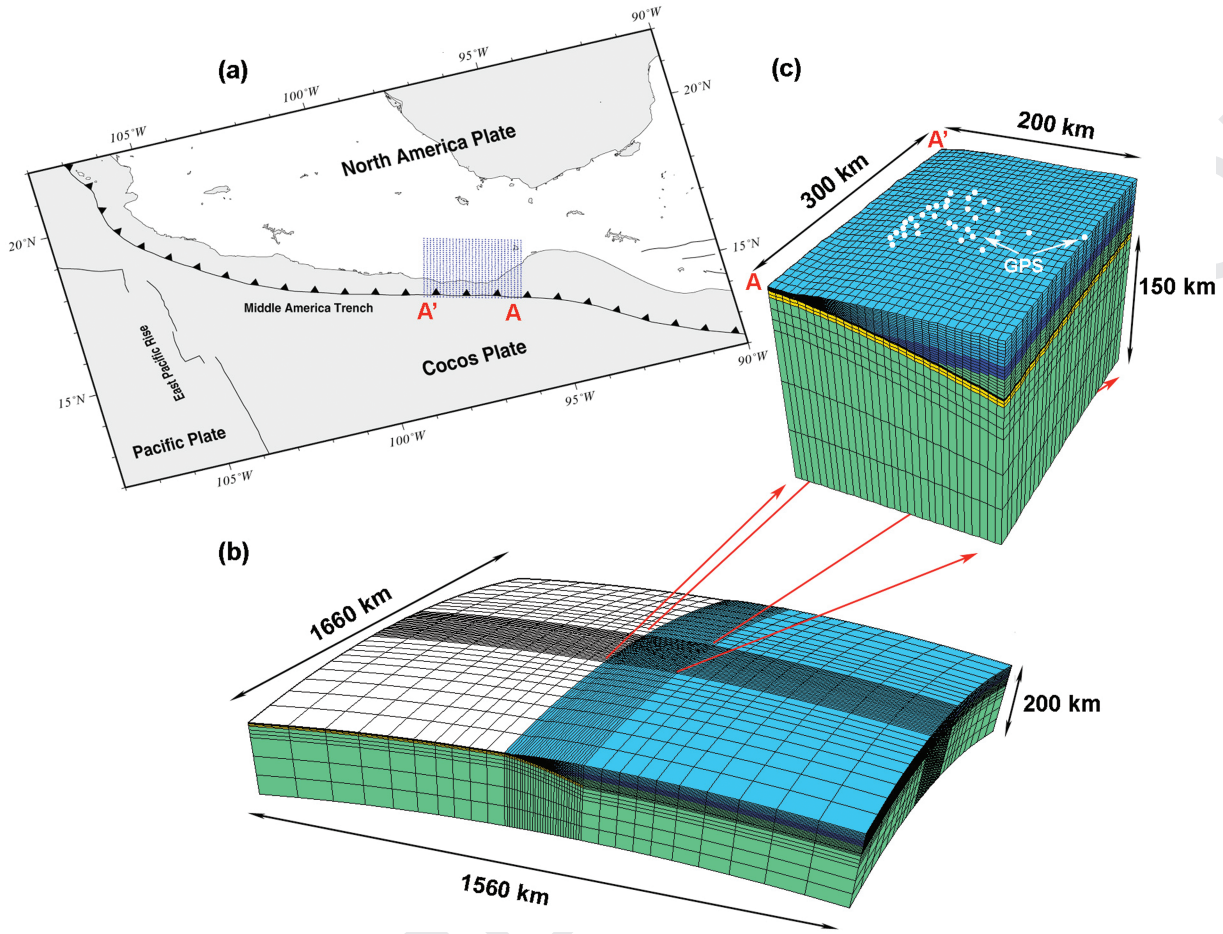

Figure 7. (a) Study area and 3-D finite element mesh. The mesh is built assuming a spherical Earth. (b) Regional mesh with lower and lateral boundaries far from the study area to avoid modelling artefacts. (c) Mesh of the study area and GPS site locations (white circles).

COLOUR FIG.

determine the best distributions of transient slip and the pattern of intertransient locking along the subduction interface beneath our study area. We estimate the magnitude of the slip or slip rate at each of the m nodes that define the subduction interface by solving the linear system $\mathbf{Gm} = \mathbf{d}$, where $\mathbf{d}$ is a $3n$-element vector that contains either the transient offsets or intertransient velocities at n GPS sites, $\mathbf{m}$ is the vector that contains the best estimate of the slip magnitude or slip rate at each node at the subduction interface and $\mathbf{G}$ is a $3n \times m$ matrix. The Green's function matrix $\mathbf{G}$ is made via forward modelling with the FEM and represents the elastic response at each GPS station for a unit displacement or unit slip rate at each node at the subduction interface.

The inverse problem takes the following form:

$$\begin{bmatrix} \mathbf{WG} \\ \alpha\mathbf{F} \end{bmatrix} \mathbf{m} = \begin{bmatrix} \mathbf{Wd} \\ 0 \end{bmatrix}, \tag{1}$$

where α is the smoothing coefficient, $\mathbf{F}$ is the smoothing matrix and $\mathbf{W}$ is a square diagonal weighting matrix that contains the reciprocal of the data uncertainties. The smoothing constraints $\alpha\mathbf{F}$ are treated as pseudo-data and are applied in both the downdip and along-strike directions.

During each inversion, we also calculate the model resolution matrix $\mathbf{R}_{\boldsymbol{m}} = \mathbf{G}^{\#}\mathbf{G}$ and data resolution $\mathbf{R}_{\mathrm{d}} = \mathbf{G}\mathbf{G}^{\#}$ (Aster *et al.* 2005), where $\mathbf{G}^{\#} = (\mathbf{G}^{\mathrm{T}}\mathbf{G} + \alpha^2\mathbf{F}^{\mathrm{T}}\mathbf{F})^{-1}\mathbf{G}^{\mathrm{T}}$. The former quantity specifies the degree to which the model is able to resolve the intertransient degree of locking or transient slip magnitudes as a function of location along the subduction interface. The diagonal elements of $\mathbf{R}_{\mathrm{d}}$ represent the amount of information that individual data contribute to the solution and are tabulated as data importances in Table 1.

For all of the inversions, we define the best-fitting model as the model with the smoothing coefficient α and model vector $\mathbf{m}$ that minimizes χ^2_ν (i.e. χ^2/dof), where the degrees of freedom (dof) are defined by Hansen (1992) as follows:

$$\mathrm{dof} = \mathrm{trace}[\mathbf{I} - \mathbf{G}(\mathbf{G}^{\mathrm{T}}\mathbf{G} + \alpha^2\mathbf{F}^{\mathrm{T}}\mathbf{F})^{-1}\mathbf{G}^{\mathrm{T}}]. \tag{2}$$

Substituting the definition for the data resolution $\mathbf{R}_{\mathrm{d}}$ from above into (2) yields an alternative, more useful expression for the degrees of freedom in terms of the number of data [trace($\mathbf{I}$)] and the number of estimated parameters [trace($\mathbf{R}_{\mathrm{d}}$)], as follows

$$\mathrm{dof} = \mathrm{trace}(\mathbf{I} - \mathbf{R_d}) = \mathrm{trace}(\mathbf{I}) - \mathrm{trace}(\mathbf{R_d}). \tag{3}$$

The χ^2_ν criteria defined above is a powerful means for identifying the optimal trade-off between the improvement in the fit of a given model versus the number of model parameters that are used to achieve that fit in the presence of smoothing for underdetermined problems.

For our inversions of the measured transient offsets, we employ a non-negative least-squares approach to enforce a uniform sense of slip during each episode of transient slip (Lawson & Hanson 1974).

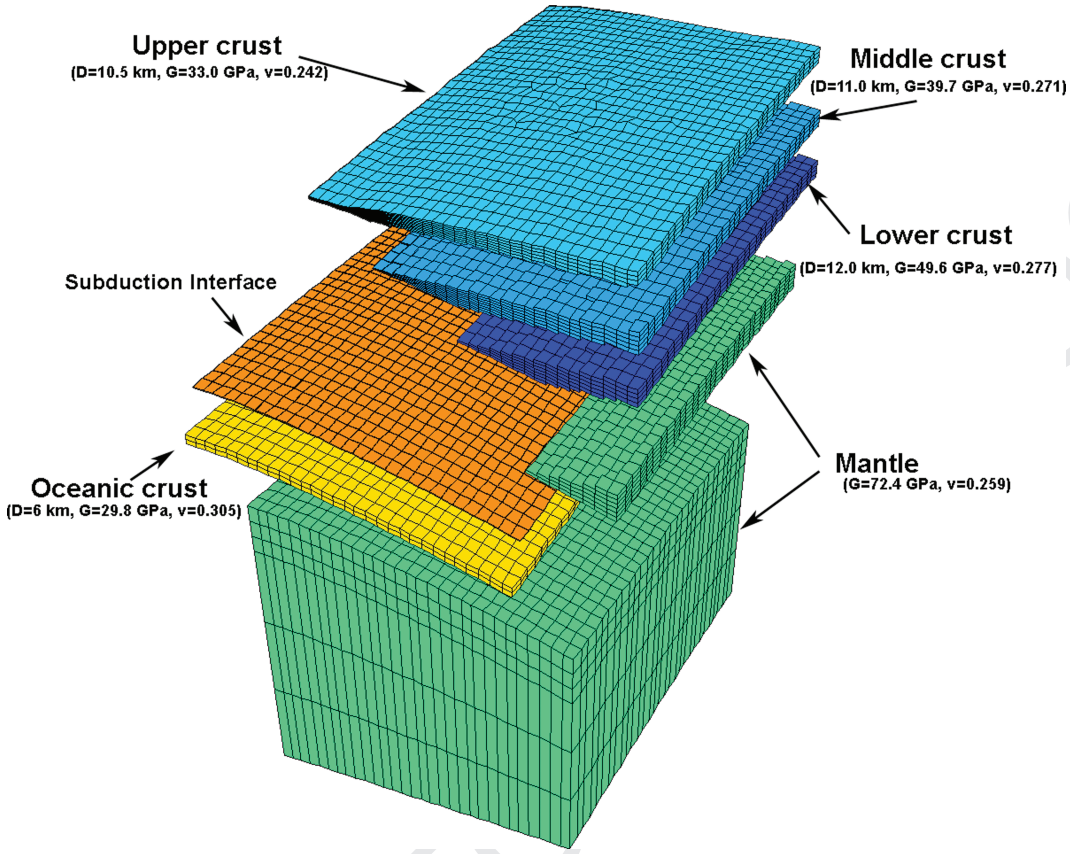

COLOUR FIG.

Figure 8. Expanded view of the mesh. The upper surface is defined by continental topography and seafloor bathymetry from Smith & Sandwell (1997) . Thickness (D), shear modulus (G) and Poisson's ratio (ν) for each layer are derived from seismically-based CRUST2 model (Bassin *et al.* 2000, Table 2). All lateral and base nodes in the extended mesh are pinned.

Table 2. Material properties and layer thicknesses of the finite element model.

Layer	Thickness (km)	V_P (km s^{-1})	V_S (km s^{-1})	ρ (kg m^{-3})	ν	G (GPa)	E (GPa)
Upper crust	10.5	6.0	3.5	2700	0.242	33.0	82.1
Middle crust	11.0	6.6	3.7	2900	0.271	39.7	100.9
Lower crust	12.0	7.2	4.0	3100	0.277	49.6	126.6
Oceanic crust		6.1	3.2	2900	0.305	29.8	77.7
Mantle		8.1	4.6	3300	0.259	72.4	182.3
Sediments					0.150	21.7	50.0

Note: Properties for the continental crust and mantle are defined at a point located at the centre of the mesh (16.5°N, 96.8°W) and for the oceanic crust values at a point near the trench (15.0° N, 100.0° W). Poisson's ratio (ν) and shear modulus (G) are calculated from the seismic velocity model CRUST2.0 (Bassin *et al.* 2000), using the V_P and V_S wave velocities. ν and G are estimated, whereas the Young's modulus (E) can be derived by the relation $E = 2G(1 + \nu)$. Sediment properties are from Turcotte & Schubert (1982).

Q1

For our modelling of the intertransient GPS velocity field, we instead use a bounded-variable least-squares algorithm, described by Stark & Parker (1995), to enforce smoothing and sense-of-slip constraints, as was the case for our transient slip modelling and also bound the range of possible slip rates to avoid physically implausible solutions. Our intertransient modelling results are presented as dimensionless ratios of the estimated convergence-rate deficit at each mesh node along the subduction interface to the full plate convergence rate predicted at the node location. These ratios, which we refer to hereafter as the 'degree of locking', range from 0, for areas where plate convergence is accommodated by free slip, to 1, for areas with no apparent intertransient slip. We impose a lower bound of zero on the magnitude of the estimated convergence-rate deficit and an upper bound that is equal to the predicted Cocos–North America plate convergence rate (DeMets 2001).

Considerable debate surrounds the terminology that should be used to describe slip behaviour along a subduction interface, during the interseismic phase (Wang & Dixon 2004; Lay & Schwartz 2004). Our modelling provides a kinematic estimate of motion along the subduction interface. Consequently, the term 'degree of locking' conveys no explicit information about the local frictional state of the subduction interface.

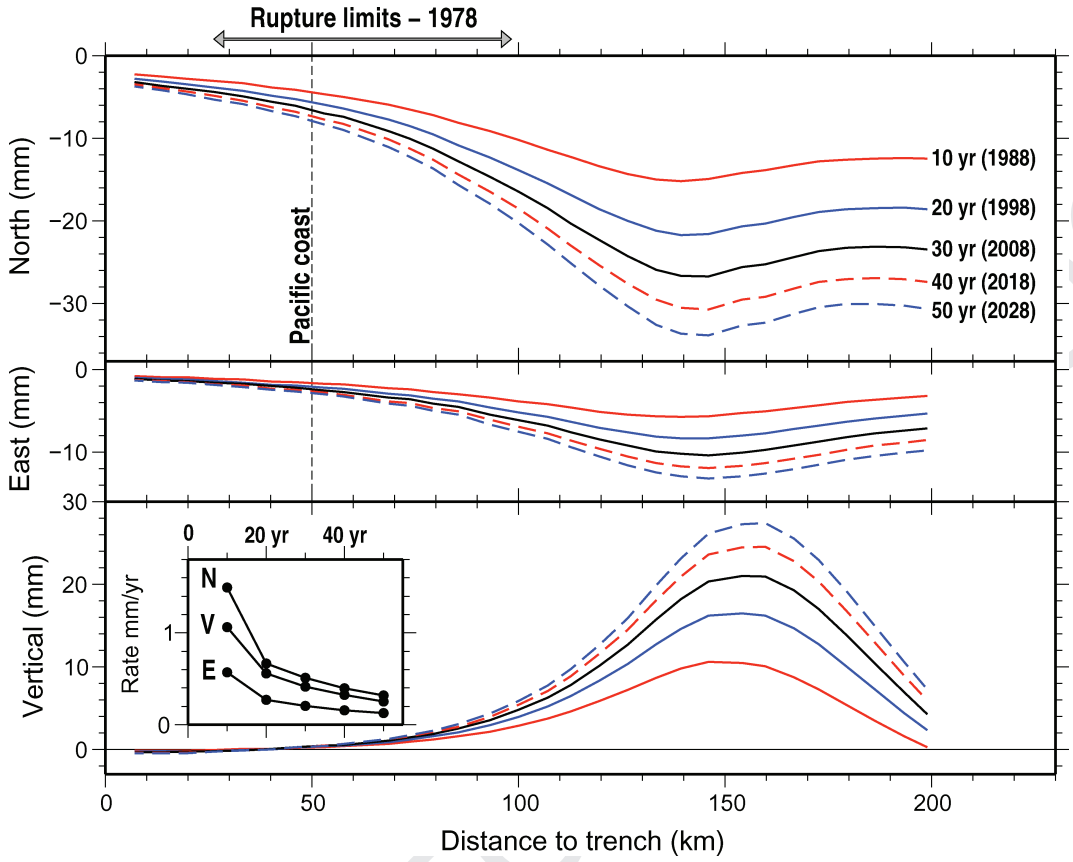

COLOUR FIG.

Figure 9. Cumulative viscoelastic displacement in north, east and vertical directions along profile B–B′ from Fig. 2, predicted for 1978 to 2028, in response to the 1978 $M_s = 7.8$ Oaxaca shallow thrust earthquake. Viscoelastic deformation is predicted using the 1978 coseismic slip distribution of Singh *et al.* (1980) and an assumed viscosity of 10^{19} Pa s for the upper mantle in the layered finite element model described in the text. Inset in the lower panel shows the change in deformation rates averaged over 10 yr intervals for the point of maximum predicted viscoelastic deformation (at roughly 150 km from the trench). Motion predicted for the period sampled by our GPS data (2001–2007) is 0.5 mm yr^{-1} or less.

3.4 Model validation and limits

We tested the mesh and our inverse code by attempting to recover two assumed distributions of intertransient slip rates, one consisting of a standard checkerboard pattern that is defined by ∼50 km alongstrike by ∼30 km downdip alternating areas of free slip and no slip (Fig. 10a) and the second consisting of a single fully locked (no slip) patch with broad gradients on its updip and downdip edges (Fig. 11a).

For the checkerboard pattern, we used the FEM to calculate synthetic surface velocities at all 31 campaign and permanent GPS locations, applying the full Cocos–North America convergence rate to each no-slip node along the subduction interface. We added Gaussian noise to the predicted surface velocities assuming typical GPS velocity uncertainties of ±1, ±2 and ±4 mm yr^{-1} for the north, east and vertical components, respectively, and inverted the noisy synthetic velocities to find their best-fitting degree of locking distribution.

Inversions of the noisy synthetic velocity field for a plausible range of smoothing coefficients show that χ^2_ν is minimized for $\alpha = 0.03$ (Fig. 10b). The corresponding best-fitting slip model (Fig. 10c) recovers the rectangular locked patch beneath the GPS network and some features of other locked patches near the network but, as expected, does not recover useful information in areas of poor station density, and hence, low model resolution. Consequently, only the locked patches that lie beneath the GPS network or within a few tens of kilometres can be resolved with any confidence.

Figs 10(d)–(f) show models that we derived using alternative smoothing coefficients, ranging from undersmoothed ($\alpha = 0.001$ in Fig. 10d) to highly oversmoothed ($\alpha = 0.3$ in Fig. 10f). All of these models successfully recover the location, magnitude and geometry of the locked patch directly beneath the GPS network. The oversmoothed solution, however, fails to recover the locations or magnitudes of any of the other locked patches and, moreover, fits the data significantly worse. The undersmoothed solution includes higher-wavelength features that were not present in the checkerboard model (Fig. 10d) and fits the data by a factor-of-five worse than the best-fitting model.

Given that transitions between no-slip and free-slip areas of the subduction interface might be broad, we also tested our ability to resolve gradients across the edges of hypothetical no- to low-slip patches (Fig. 11a). Encouragingly, we can recover most aspects of such a model (Fig. 11b). Our network geometry is thus sufficiently strong to recover either narrow (Fig. 10c) or broad (Fig. 11b) slip-rate gradients across the edges of locked patches beneath the network.

Numerical tests in which we progressively reduce the assumed size of the locked patches in the checkerboard pattern and repeat the analysis, indicate that patches as small as 20 km on a side can be resolved beneath the network, given realistic levels of GPS noise.

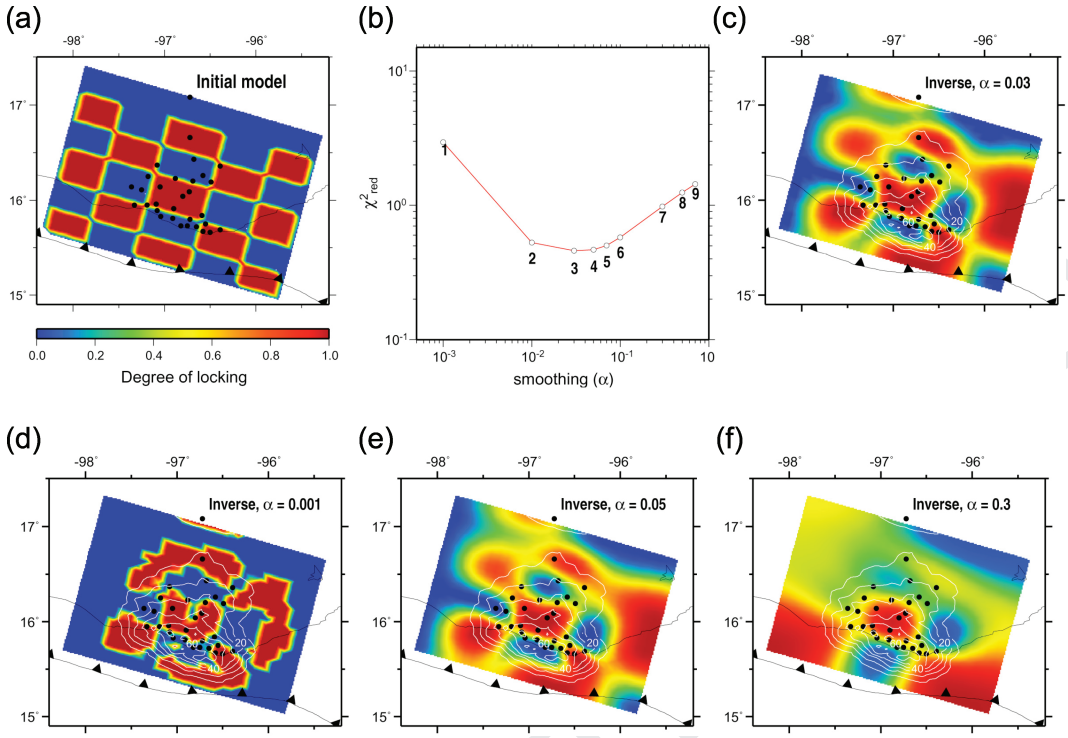

Figure 10. Test of network resolution and ability to recover a known checkerboard distribution (a) of hypothetical freely-slipping and fully-locked nodes from noisy synthetic velocities, generated at our 31 GPS station locations (filled circles). (b) Variation of fit to synthetic site velocities as function of assumed smoothing coefficient α. Numerals correspond to data inversions for different assumed values of α. (c) Preferred model with $\alpha = 0.03$, corresponding to Inversion 3 in (b). Models shown in (d), (e) and (f) correspond to Inversions 1, 4 and 7 in (b), respectively. Details about the inversion procedure and assumptions are given in the text. White contour lines show the model resolution.

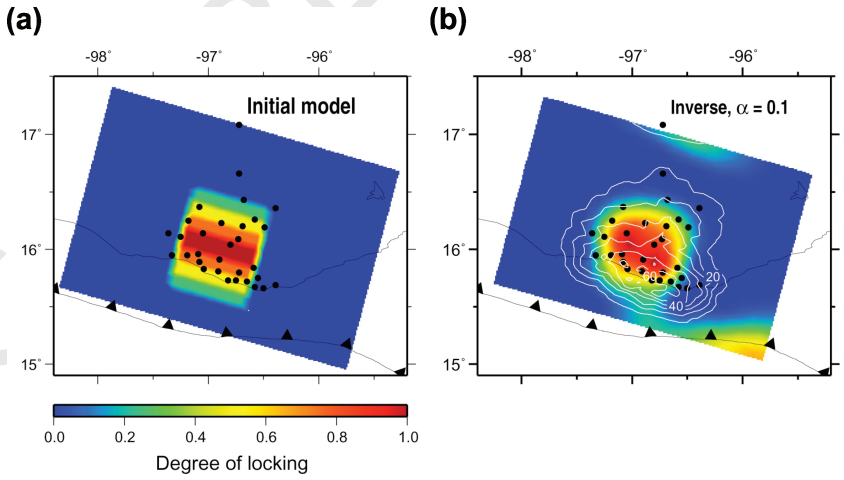

Figure 11. Test of network resolution and ability to recover a known locked path with tapered edges (a) from noisy synthetic velocities that were generated at our 31 GPS station locations, using the tapered pattern. (b) Distribution of locking estimates that best-fit the noisy synthetic site velocities. The optimal smoothing coefficient of 0.1 was determined using the same method as for the checkerboard test. Details about the inversion procedure and assumptions are given in the text. Contour lines show the model resolution.

We are unable, however, to resolve patches smaller than this with high confidence. The 10-km along-strike and 7-km downdip node spacings we use for our study area are thus smaller than the smallest slip feature on the subduction interface that can be resolved with our network and are thus sufficient for modelling our data.

Data from our GPS network can therefore be used to resolve significant variations in slip or slip rates for areas of the subduction interface that are as small as 400 km^2 and, moreover, can usefully resolve broad slip-rate gradients beneath the network. For comparison, Mazzotti *et al.* (2000) use forward and inverse modelling of synthetic data to estimate that the smallest slip patch that can be resolved along the Japan trench subduction interface with the dense Japanese continuous GPS network, is 4000–5000 km^2. The resolving capability of the Oaxaca GPS network is thus roughly an order

of magnitude better than that of the Japanese GPS array, due primarily to the factor of two-to-three greater distance that the latter array lies from its corresponding seismogenic zone than does the GPS network in Oaxaca.

4 RESULTS

4.1 Estimation and modelling of transient slip events

Q2

As a prelude to our modelling of intertransient deformation in our study area, we use our continuous GPS time-series to estimate the location and magnitude of slip during the transient slip episodes in 2004 and 2006. Following Lowry *et al.* (2001), we approximate our site coordinate time-series, using a hyperbolic tangent equation and from this estimate the north, east and vertical components of the offsets for a single transient slip event, as follows:

$$y(t - t_0) = y_0 + v * (t - t_0) + \frac{U}{2}\left[\tanh\left(\frac{t - T_0}{\tau}\right) - 1\right] \quad (4)$$

where $y(t - t_0)$ are the GPS site coordinates at time $t - t_0$, y_0 are the site coordinates at the reference time t_0, v is the steady velocity, U is the displacement that occurs during a transient event, t_0 is the median time of a transient, and τ scales the period over which a given transient event occurred. For a ∼1-yr-long window that is centred on a given transient, we seek values for U, v, τ and T_o that minimize the squared difference between the left- and right-hand sides of (4). We accomplish this using a multistage search in which we first estimate the non-linear terms t_0 and τ via a grid search for t_0 and gradient search for τ and then use a standard weighted least-squares procedure to estimate the linear terms v and U for given best-fitting values of T_o and τ.

Examples of the hyperbolic tangent fits to assorted continuous GPS time-series in 2004 and 2006 are illustrated in Figs 12(a) and 13(a). The transient offsets that we estimate from each continuous GPS time-series (Table 3) are dominantly to the south for both transient slip events, as is shown by the yellow arrows in Figs 12(b) and 13(b), and agree, within uncertainties, with the offsets that we previously estimated at these stations (Brudzinski *et al.* 2007). That the offsets at coastal stations OXPE, OXES and OXUM are systematically smaller than at the inland stations OXLP, OXMC and OAXA is qualitatively consistent with the hypothesis that the transient slip occurs along parts of the subduction interface that lie beneath the inland rather than coastal areas of the GPS network.

We inverted the six transient offsets that we measured in 2004 (Fig. 12b and Table 3) to estimate the distribution of slip along the subduction interface during this transient slip episode (Fig. 12c). A systematic search for the direction of transient slip that gives rise to the best overall fit yielded a best downdip direction of N15°E. In areas of the subduction interface where our model resolution is good and the slip magnitudes are thus more reliably determined (indicated by the areas enclosed within the dashed line in Fig. 12c), the transient slip is located almost exclusively below depths of 20 km (Fig. 14a) downdip from the lower limit of seismogenic rupture in 1978. The slip that occurred during the 2004 transient has an equivalent moment magnitude of $M_W = 6.6$.

Our best-fitting estimate for the distribution of transient slip in 2004 is remarkably similar to the distribution of slip that we derived in a previous study of this slip transient (Brudzinski *et al.* 2007), despite the different subduction interface geometries and transient offsets that are employed in the two studies. The only notable difference between the results reported by the two studies is the maximum slip magnitude. The maximum slip amplitude that we estimate in this study, 115 mm, is nearly 50 per cent smaller than we found previously (220 mm; Brudzinski *et al.* 2007). This difference is caused by the different subduction interface geometries that are employed in the two studies. Our earlier study employs a geometry that places the subduction interface deeper beneath the GPS network at inland locations than does the shallower interface geometry employ herein. Significantly higher slip amplitudes are required for this deeper interface geometry than is the case for the the shallower interface geometry to generate equivalent amounts of elastic deformation at the surface. The same effect explains the difference in moment magnitudes that are estimated for the 2004 transient slip episode here ($M_W = 6.6$) and in our previous study ($M_W = 7.3$).

Although our ability to resolve the details of transient slip in 2006 was degraded due to equipment malfunctions at the inland sites OXMC and OXLP (compare the model resolution contours in Figs 12c and 13c), our inversion of the four transient offsets that we measured in 2006 (Fig. 13b), nonetheless, yields a best-fitting distribution of transient slip along the subduction interface (Fig. 13c) that strongly resembles the 2004 slip solution in all respects. The best-fitting downdip direction (N15°E), maximum slip amplitude (100 mm) and equivalent moment magnitude ($M_W = 6.6$) that we estimate for the 2006 transient slip episode are the same within the uncertainties as for the 2004 transient slip episode. The estimated locations of transient slip in 2004 and 2006 are also the same within uncertainties (Figs 14a and c), with most slip during both episodes concentrated at depths below the seismogenic zone (i.e. below 18–20 km) and downdip from the 1978 earthquake rupture zone.

Our new estimate of the distribution of transient slip in 2006 differs significantly from that of Brudzinski *et al.* (2007), who inverted transient offsets from the same four stations as are treated here and six additional GPS stations in the Mexican volcanic belt and Guerrero to estimate the cumulative distribution of transient slip beneath southern Mexico, in 2006. Modelling that we are presently engaged in indicates that two distinct transients occurred in 2006, one beneath Oaxaca in early 2006, which is modelled here, and a second beneath the state of Guerrero in the latter half of 2006 (Larson *et al.* 2007). Our new model for the slip transient in early 2006 (Fig. 13c) is derived solely from transient offsets that occurred at GPS stations in Oaxaca in early 2006 and thus is likely to portray more accurately this slip transient than does the model reported by Brudzinski *et al.* (2007).

Our best-fitting distributions of transient slip in 2004 and 2006 have similar locations and amplitudes. Both suggest that transient slip occurred principally downdip from the seismogenic zone that is defined by the rupture limits of previous earthquakes in this region (Figs 14a and c), although the sparser station coverage in 2006 precludes us from estimating a firm limit on the updip extent of transient slip.

We did not attempt to estimate or correct our GPS station time-series for the effects of the transient slip events in late 2001 and mid-2002, primarily because too few observations are available with which to model either event. The lack of any correction for either of these transient slip events biases the transient-corrected interseismic site velocities that we describe in the following section and hence represents a limiting factor in our analysis of the nature of intertransient locking of the subduction interface. A consideration of the likely effect of this bias on our estimated intertransient station velocities based on the magnitudes of the transients in 2001 and 2002 suggests that it is no more than 5 per cent at a given site,

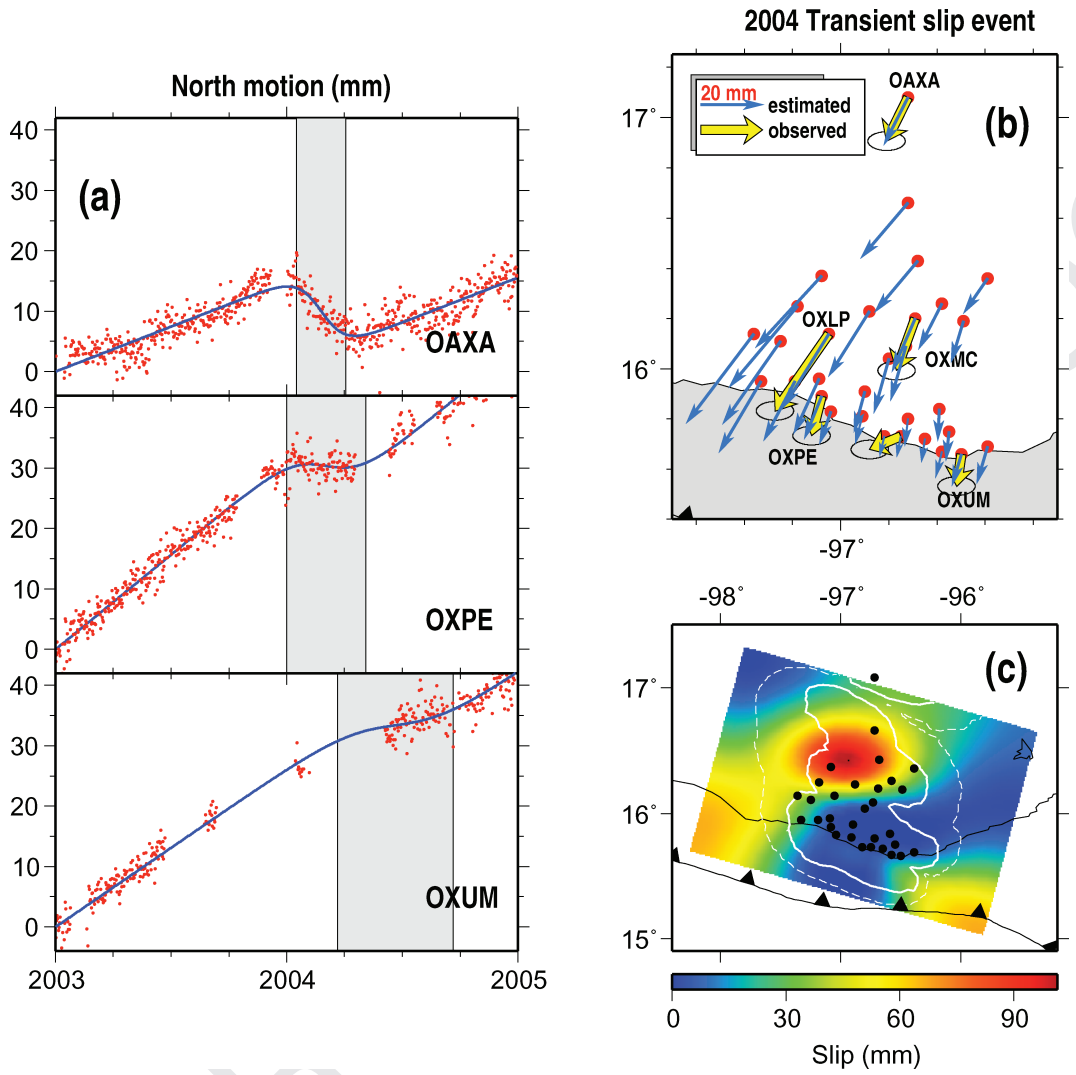

Figure 12. Observations and modelling of 2004 transient slip event. (a) North components for three continuous GPS stations in the study region relative to North America plate. Grey bars show the timing for the 2004 slow slip event. Blue lines are the best-fitting hyperbolic tangent fits to the GPS time-series. (b) Station displacements during the 2004 transient slip event. Yellow arrows show the transient offsets for continuous GPS stations, determined from hyperbolic tangent fits, to their time-series. Blue arrows indicate the station motions that are predicted from the transient slip distribution that best fits the transient offsets measured at the continuous sites. (c) Best-fitting distribution of slip during the 2004 transient. White contour lines show model resolution for 1 per cent (dashed) and 5 per cent (solid). A 3-D image of the slip patch, including its depth, is shown in Fig. 14(a).

too small to alter substantially any of the primary results that are presented below.

4.2 Estimation and modelling of intertransient deformation

4.2.1 Observed intertransient velocity field

To estimate the degree of locking along the subduction interface between transients, we use the best-fitting models for transient slip in 2004 and 2006 (Figs 14a and c) as a basis for estimating and removing the effect of both transients on all of the GPS coordinate time-series. We accomplish this by using our FEM and the best-fitting models for transient slip in 2004 and 2006 to predict the elastic surface displacements that occurred during each transient event at each GPS site (blue arrows in Figs 12b and 13b). We then use these displacements, which vary smoothly through the study area and obey the elastic constraints that are imposed by our inversions of the sparse continuous GPS time-series, to correct each campaign (and continuous) coordinate time series prior to estimating their best-fitting slopes and intercepts.

Fig. 6 illustrates the effect of the 2004 and 2006 transient corrections at the continuous GPS station OXPE along the Oaxacan coast. A linear regression of the uncorrected time-series (upper left-hand panel) yields a slope of 21.7 ± 1.5 mm yr^{-1} and χ^2_ν of 2.2. The normalized misfit is more than a factor of two greater than the value of $\chi^2_\nu = 1$ that would be expected for a purely linear time-series with Gaussian noise. In contrast, a linear regression of the corrected coordinate time-series yields a best-fitting rate of 30.1 ± 2 mm yr^{-1}, nearly 50 per cent faster than before, and χ^2_ν of 1.1, close to that expected for linear station motion.

Similar to OXPE, the other corrected station velocities (Fig. 6b) are systematically faster than their uncorrected counterparts (Fig. 6a) and are rotated on average by 1.4° counter-clockwise,

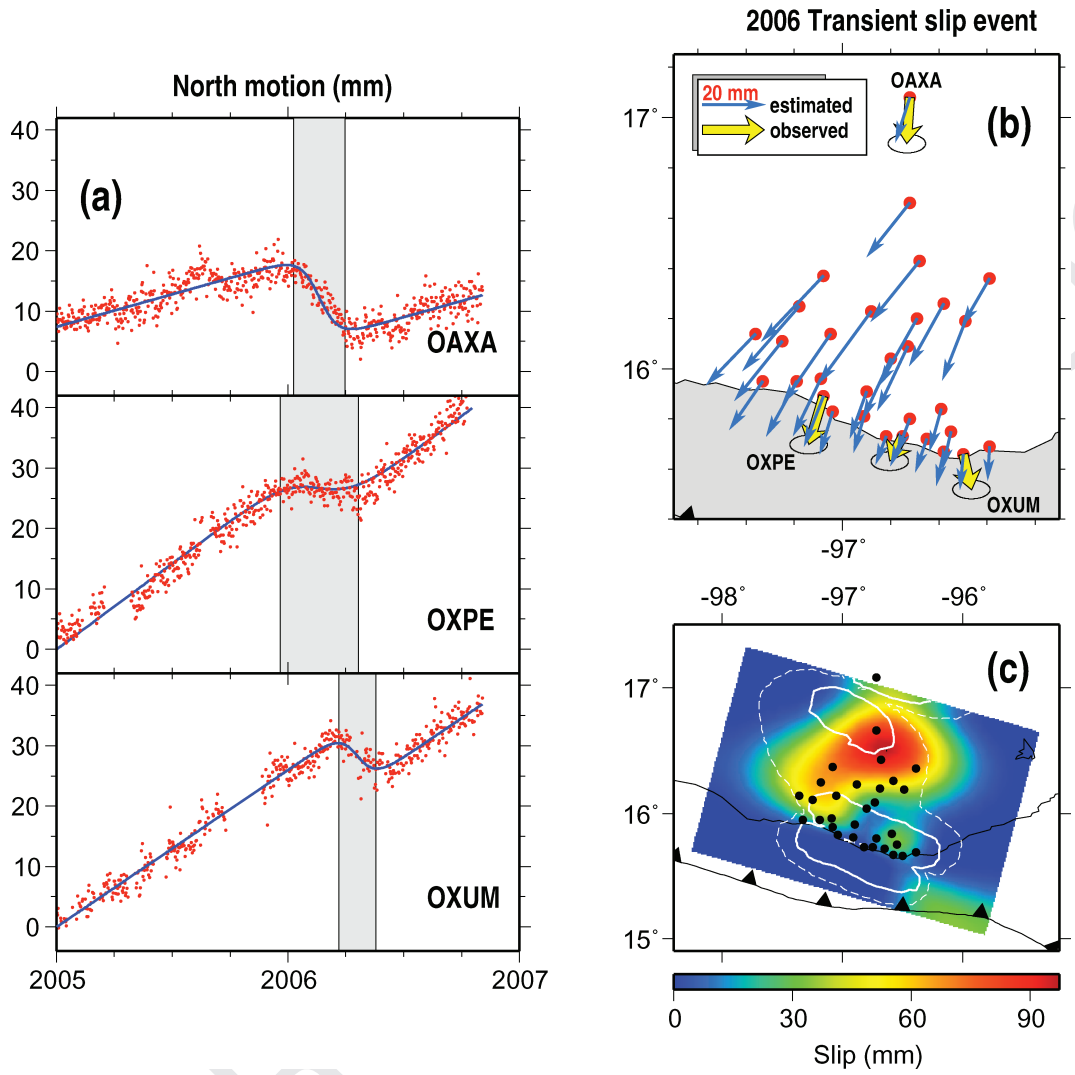

COLOUR FIG.

Figure 13. Observations and modelling of 2006 transient slip event. (a) North components for three continuous GPS stations in the study region relative to North America plate. Grey bars show the timing for the 2006 slow slip event. Blue lines are the best-fitting hyperbolic tangent fits to the GPS time-series. (b) Station displacements during the 2006 transient slip event. Yellow arrows show the transient offsets for continuous GPS stations, determined from hyperbolic tangent fits, to their time-series. Blue arrows indicate the station motions that are predicted from the transient slip distribution that best fits the transient offsets measured at the continuous sites. (c) Best-fitting distribution of slip during the 2006 transient. White contour lines show model resolution for 1 (dashed) and 5 per cent (solid). A 3-D image of the slip patch, including its depth, is shown in Fig. 14(c).

Table 3. Characteristics of transient slip events at continuous GPS sites.

Event	Site	T_o (yr)	τ (yr)	U_{north} (mm)	U_{east} (mm)	U_{up} (mm)	V_{north} (mm yr^{-1})	V_{east} (mm yr^{-1})	V_{up} (mm yr^{-1})
2004	OAXA	2004.1493	0.1061	−14.2	−7.0	−6.4	14.9	11.0	−0.6
2004	OXES	2004.1713	0.1708	−4.2	−10.1	−20.6	32.4	14.8	−13.2
2004	OXPE	2004.1713	0.1708	−12.7	−3.2	−2.9	31.4	19.9	−7.4
2004	OXUM	2004.4699	0.2500	−10.4	−1.5	−17.4	26.3	16.5	−1.9
2004	OXLP	2004.1493	0.1061	−25.0	−17.4	31.7	29.5	21.7	−22.8
2004	OXMC	2004.0781	0.1126	−16.8	−6.1	24.0	27.7	18.5	−20.5
2006	OXES	2006.2424	0.0958	−8.0	−4.2	17.5	32.3	17.1	-13.3
2006	OXUM	2006.3000	0.0790	−11.5	2.7	9.7	26.8	8.6	-16.5
2006	OAXA	2006.1356	0.1108	−15.0	−1.0	4.0	10.9	−0.9	−4.7
2006	OXPE	2006.1356	0.1689	−15.6	−4.7	23.6	33.9	21.7	−25.2

Note: Transient slip characteristics are estimated from hyperbolic tangent fit (Section 4.1). T_o is the median time; τ scales the period over which the event occurred; U_{north}, U_{east} and U_{up} are displacements during transient. Displacements must be divided by two for comparison to 2004 and 2006 transient displacements from Brudzinski *et al.* (2007). Velocities are best-fitting estimates for 1-yr-long windows that are centred on their respective transients.

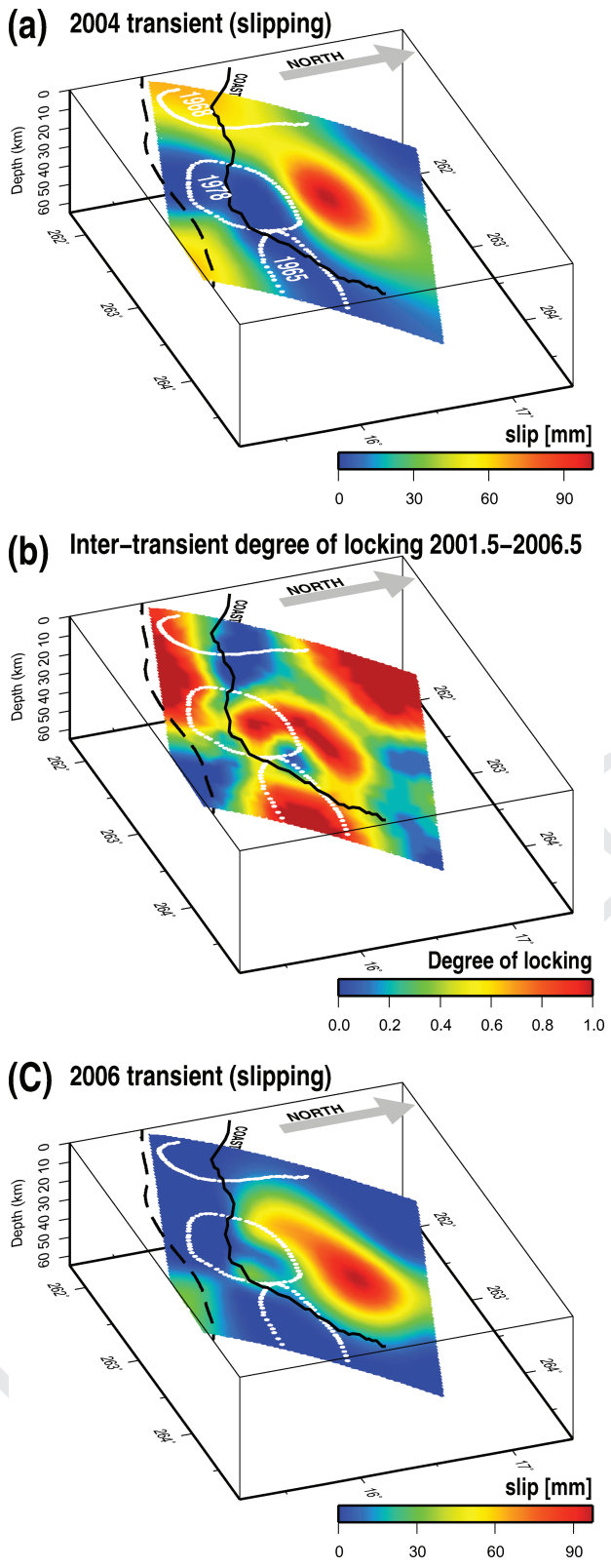

Figure 14. 3-D view of the subduction interface showing the best-fitting distributions of slip during the 2004 (a) and 2006 (c) transient slip events and the best-fitting distribution of the intertransient degree of locking (b). White-dashed lines indicates rupture zones of the 1965, 1968 and 1978 subduction thrust earthquakes (Singh *et al.* 1980; Tajima & McNally 1983). Black dashed line shows trace of the Middle America trench.

COLOUR FIG.

relative to their uncorrected directions. The average direction of motion of the corrected velocity vectors, N32.5 ° E ± 1°, is the same within uncertainties as the N31.8E ° ± 1.2° direction predicted at this location for Cocos–North America motion (DeMets 2001). In contrast, the average uncorrected direction of N35.2° E ± 1° is rotated significantly clockwise from the predicted plate convergence direction. The improved agreement between the estimated plate convergence direction and corrected GPS station directions indirectly validates the correction we make to the station velocities for transient slip.

The vertical components of the station motions are dominantly downward (Figs 15b and 16b). Rapid subsidence along the coast changes gradually inland to insignificant vertical motion and then slow uplift at the sites farthest inland. In most subduction settings, the transition at the surface between regions of uplift and subsidence in the overlying plate is located above the transition at depth between freely slipping and locked areas of the subduction interface. That the transition in the sense of vertical motion in our study area is located approximately 70–80 km inland from the coast (Fig. 15b) implies that most of the GPS network lies above locked areas of the subduction interface.

4.2.2 Forward and inverse modelling of the intertransient velocity field

The intertransient station rates from three trench-normal transects of the study area (Fig. 15) illustrate several important features of our velocity field. GPS sites from a transect that passes through the centre of the network move inland systematically faster than do sites that lie within transects of the eastern and western areas of our network (Fig. 15a) and therefore imply a higher degree of locking along the subduction interface beneath the centre of the network. Most of the GPS site rates fall between the rates that are predicted by simple forward models in which we impose either a no-slip (fully locked) or 50 per cent free-slip condition along the entire seismogenic zone. That neither of these two simple forward models is able to match the observed patterns in the horizontal or vertical GPS rates implies that a model that incorporates along-strike and downdip variations in the degree of locking along the subduction interface is needed to fit the data.

We inverted the intertransient GPS site velocities using techniques described in Section 3.3 to identify the pattern of intertransient locking of the subduction interface that yields the best least-squares fit to the data (Fig. 16c). The normalized misfit χ^2_ν for the best-fitting model is 0.95 for the optimal smoothing coefficient that we identified. The 3-D GPS station velocities are therefore fit to within a few percent of their estimated uncertainties. The horizontal station motions, which contribute 60 per cent of the total data importance, are well fit (Fig. 16a) and show no obvious pattern in their residual velocities (Fig. 16d). The vertical rates, which contribute the remaining 40 per cent of the data importance, are also fit (Fig. 16b) within their larger uncertainties. We view it as encouraging that the model successfully captures the patterns of both the vertical and horizontal deformation, without compromising the overall fit (as indicated by the low value for χ^2_ν). This suggests that the horizontal and vertical velocity components are mutually consistent, and that intertransient deformation in this region is well described.

The estimated degree of locking for the best-fitting intertransient solution (Fig. 16c) ranges from 60 per cent to 100 per cent of the full plate convergence rate beneath much of the GPS network. Areas with high locking values coincide with the rupture zone of the 1978

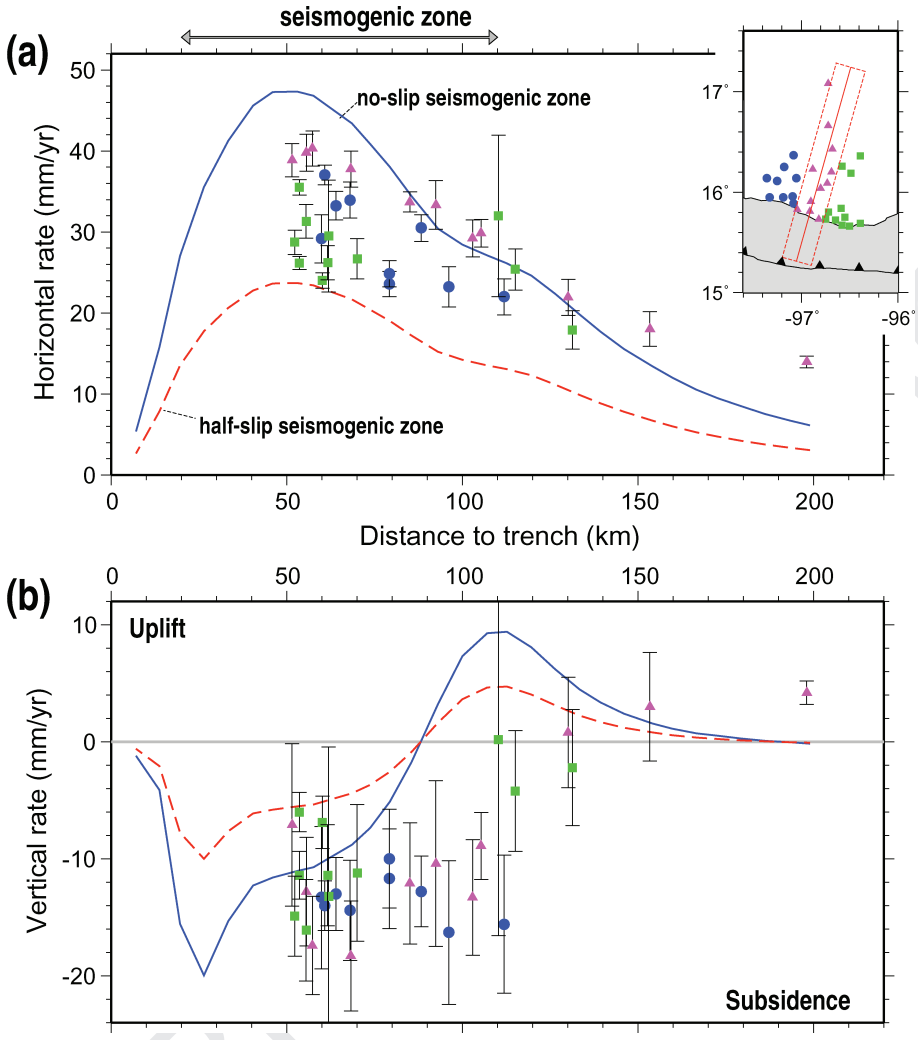

Figure 15. Comparison of measured (a) horizontal and (b) vertical intertransient GPS rates along three trench-normal transects of the Oaxaca GPS network with rates that are predicted from forward modelling, using our layered finite element model. Transect locations are indicated in the inset, with blue circles, magenta triangles and green squares representing GPS stations within the western, central and eastern transects, respectively. Predictions for two assumed models are shown: blue curve shows surface deformation rates for full locking of the seismogenic zone, whose up- and downdip limits are defined, respectively, by the 100 and 350 °C isotherms modelled by Currie *et al.* (2002). The red-dashed curve shows surface deformation rates for 50 per cent locking of the seismogenic zone. Vertical error bars show 1σ rate uncertainties.

COLOUR FIG.

Oaxaca earthquake but also extend farther downdip into the region where transient slip events occur (Fig. 14). Although areas of high locking also extend updip to the northwest, along-strike to the east and farther downdip from the region of transient slip (Figs 14 and 16c), these are located in regions of low or no model resolution and are thus poorly resolved by our data.

4.2.3 Evidence for significant variations in locking

Our best-fitting model indicates that the degree of locking varies significantly in both the along-strike and downdip directions beneath the study area (Fig. 17). We examined whether the variations in locking along the subduction interface coincide with changes in the surface deformation for a trench-parallel transect (A–A* in Figs 17a–c) and trench-normal transect (B–B* in Figs 17a, d and e) of the GPS network.

Along the coastal transect A–A*, where the station coverage is dense and the deformation pattern is well determined, the GPS site rates change significantly between stations OXLU and OXPA (Fig. 17b). The site rates increase steadily from 28 ± 4 mm yr^{-1} at the western end of the profile to 38–40 mm yr^{-1} along a 30-km-long stretch of the coast between stations OXZI and OXAB and then decrease steadily eastward along the transect to only 24 ± 1.5 mm yr^{-1} at the eastern end of the profile. The changes in the site rates along this profile are several times larger than the standard errors in the site rates and are thus highly significant.

Along the same profile, the degree of locking shows a pattern similar to that exhibited by the site rates (red lines in Figs 17b and c). Locking increases steadily from a low of only 10 per cent at the western end of the profile to a peak of 65 per cent near the centre of the profile and then decreases steadily to 30 per cent at the eastern end of the profile. Differences in the locations of the maximum rates and locking along this profile are caused by the requirement that the best-fitting model also fit GPS site velocities farther inland. Based on this comparison, we conclude that apparent changes in the degree of locking along the coast are driven by highly significant

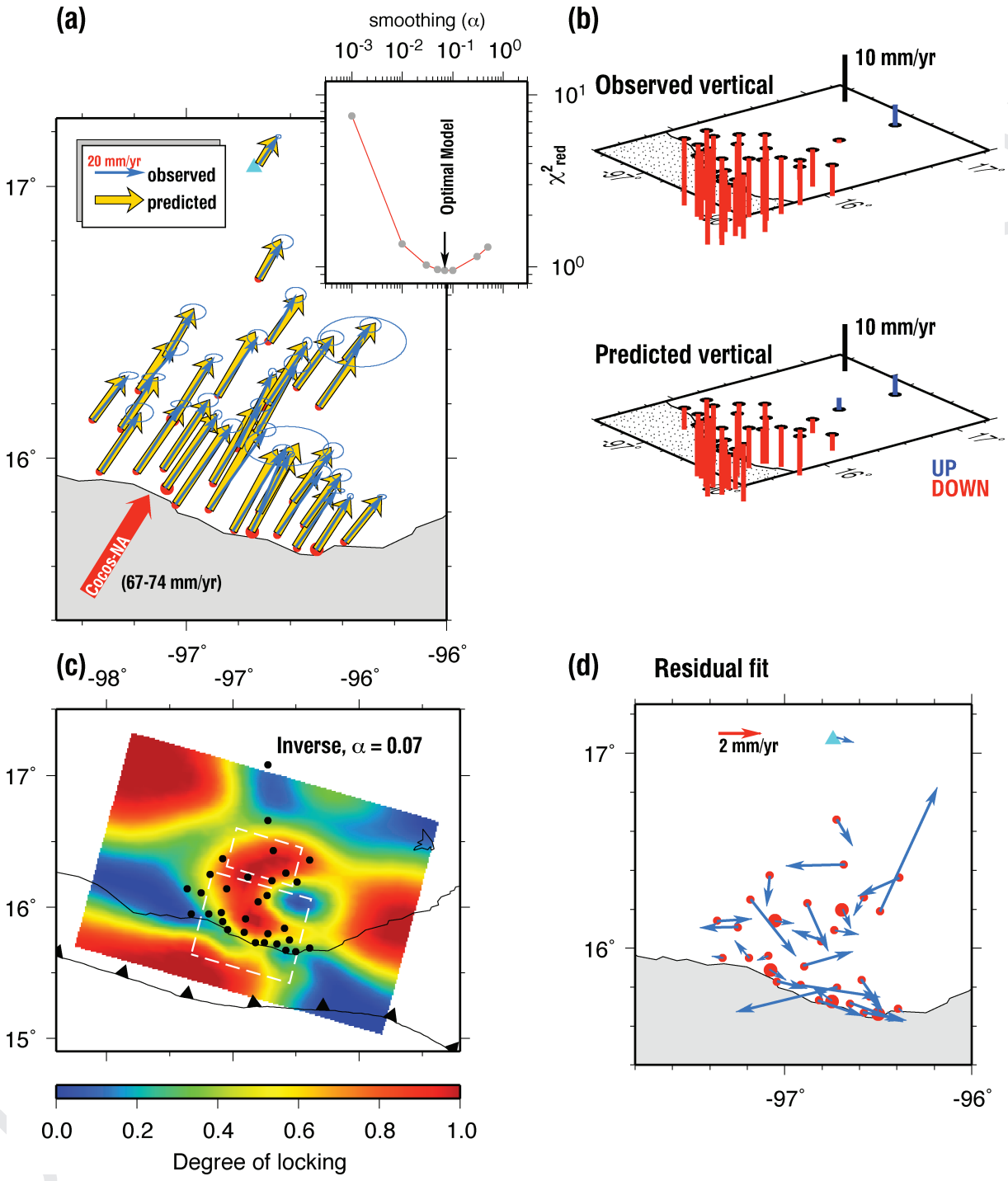

Figure 16. (a) Observed (yellow) and predicted (blue) horizontal GPS station velocities relative to North American plate after correcting for the effects of the 2004 and 2006 transient slip events. Inset indicates values of χ^2_ν for a range of smoothing coefficients. (b) Observed (upper) and predicted (lower) vertical station rates for the best-fitting inverse model. (c) Degree of locking for the best-fitting model. Fig. 14(b) shows a 3-D view of the intertransient locking distribution. Circles indicate GPS site locations. Dashed lines show areas selected for elastic energy calculations along the seismogenic and transitional zones (Section 5.2). (d) Residual fit for the best-fitting slip distribution shown in (c), calculated by subtracting the observed site velocities from the predicted velocities. Uncertainty ellipses are omitted for clarity.

COLOUR FIG.

differences in the GPS site rates from coastal areas of the study area and are therefore real.

Along the trench-normal transect B–B* (Figs 17d and e), both the horizontal and vertical site rates decrease rapidly between the coast and inland areas. Fitting the pattern of observed rates requires that the subduction interface beneath the transect remain fully locked to distances 70 km inland from the coast (red lines in Figs 17d and e), significantly farther inland than the downdip limit of the 1978 earthquake rupture zone. The GPS rates, therefore, require that areas of the subduction interface where transient slip occurred

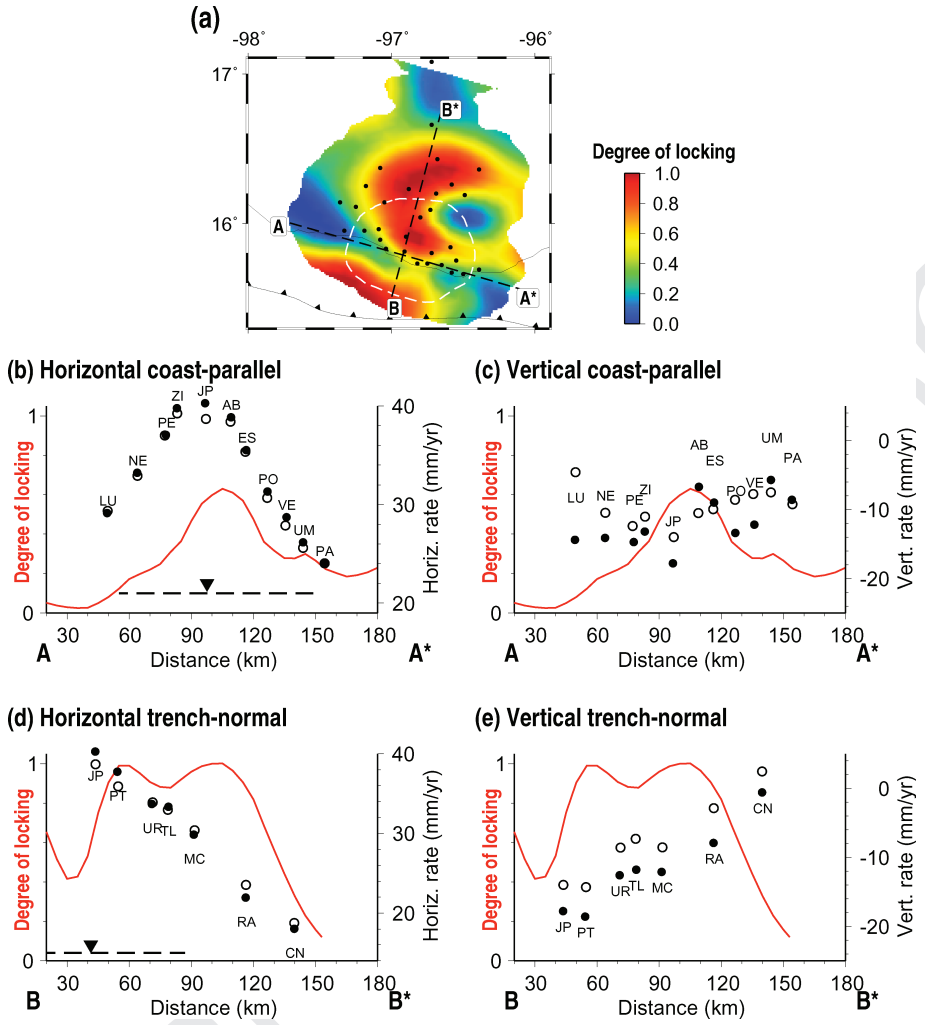

Figure 17. (a) Best-fitting distribution of interseismic locking from Fig. 16(c) but excluding areas of the subduction interface with poor model resolution. White-dashed line shows 1978 earthquake rupture limits. (b) and (c) show the estimated degree of locking (red curve), observed GPS rates (filled circles) and predicted GPS rates (open circles) for all sites that are located within 10 km of the trench-parallel profile A–A*. Panels (d) and (e) show the same information for GPS sites that are located within 15 km of the trench-normal profile B–B*. Observed GPS rates are the same as are shown in Figs 15 and 16. Horizontal dashed lines in (b) and (d) show the limits of the 1978 earthquake rupture zone, and inverted triangles show where profiles A–A* and B–B* intersect. Rate uncertainties are omitted for clarity.

COLOUR FIG.

in both 2004 and 2006 were fully locked between those transient slip episodes. In Section 5.2, we demonstrate that the elastic strain that accumulated between late 2002 and 2006 across the locked zone downdip from the seismogenic zone appears to have been fully relieved by transient slip during the 2004 and 2006 transient slip events.

4.2.4 Influence of the assumed subduction interface geometry

We tested the influence of the geometry that we assume for the subduction interface by repeating the velocity field inversion, using a mesh that incorporates the sub-horizontal interface geometry described by Franco *et al.* (2005); see Fig. 3(b). The normalized least-squares misfit (χ^2_ν) increases by ∼40 per cent for a best-fitting model that is derived with this alternative geometry, with most of the increased misfit caused by poor fits of the model to the velocities for two of our inland sites. Despite the worse fit at these two sites, the pattern of intertransient locking for this geometry is remarkably similar to that for our best-fitting model. Our conclusions are thus robust with respect to either interface geometry. Additional tests in which we varied the dip of the seismologically-based interface by ±5° also resulted in no significant change to the resulting pattern of locking along the subduction interface.

5 DISCUSSION AND CONCLUSIONS

5.1 Relative locations of transient slip and the seismogenic zone

An important unresolved question regarding the Mexican subduction zone is whether transient slip intrudes upward into the seismogenic zone and hence may relieve some fraction of the interseismic elastic strain that is accumulating along different segments of the trench. Detailed studies of transient slip during the $M_W = 7.5$ silent earthquake of 2001–2002 along the Guerrero segment, west of Oaxaca, indicate that most slip occurred at depths of 25 km or deeper, below the seismogenic zone, but also suggest that some slip intruded upward into the seismogenic zone (Kostoglodov *et al.*

2003; Iglesias *et al.* 2004; Yoshioka *et al.* 2004). Slip during the 2006 $M_W = 7.5$ transient slip event in the Guerrero region was focused primarily downdip from the seismogenic zone, but also may have included minor slip at shallower levels (Larson *et al.* 2007).

The 2004 and 2006 transient slip events beneath Oaxaca exhibit little or no overlap with the rupture limits of previous large earthquakes in this region (Figs 14a–c), irrespective of the interface geometry that we use for our modelling. In particular, the transient offsets that we recorded in 2004 at our continuous sites OXLP and OXMC are fit poorly if we attempt to force transient slip in our model to shallower levels of the subduction interface. Transient slip thus, almost certainly, did not extend updip into the seismogenic zone in 2004 (Fig. 12).

Our results therefore suggest that non-overlapping seismogenic and transitional slip regions exist beneath our study area, and that little or no slip from the deeper transitional region intrudes upwards into the seismogenic zone. Improved station coverage is needed to determine whether the the seismogenic and transitional regions elsewhere in southern Mexico are similarly decoupled.

5.2 Intertransient strain accumulation and release in Oaxaca

Based on a synthesis of seismologic observations of shallow earthquake ruptures, Pacheco *et al.* (1993) propose that subduction interfaces consist of strongly locked asperities conducive to seismogenesis and weakly locked regions where some combination of stable sliding and slow slip phenomena accommodate some or all of the plate convergence. The evidence described above for the most rapid surface deformation along the coast above the core of the 1978 earthquake rupture zone and deformation rates that decrease towards the edges of the rupture zone is consistent with such a model (Figs 14b and 17b).

Our observations and modelling also clearly show that the subduction interface is strongly coupled downdip from the seismogenic zone, where transient slip occurs (Fig. 14). One question relevant to the long-term accumulation and release of elastic strain during major ruptures of the seismogenic zone is whether any elastic energy from locking of the deeper zone of transient slip might contribute to the total energy release during a major subduction zone earthquake. We therefore compared the total elastic energy that accumulated and was released across the deep transition zone (area indicated by dashed line in Fig. 16c) between 2002.85 and 2006.3, comprising two full transient slip cycles. From the estimated degree of locking and known plate convergence rate, the elastic energy that accumulated during this period across the deep transition zone was 2.7×10^{19} N m. For comparison, the total energy that was released by the 2004 and 2006 transient slip events for the same area was 2.1×10^{19} N m. Within the uncertainties, the elastic energy that was released during the two transients that occurred in this 3.5-yr-long period was approximately in balance with the elastic energy that accumulated prior to those transients. If the elastic energy budget is similarly balanced for the entire seismic cycle, then little or no potential elastic energy is stored along the deep locked zone between major earthquakes.

5.3 Comparison to other results

5.3.1 Mexican subduction zone

Only one other study of interseismic strain accumulation along the Oaxaca segment of the Mexican subduction zone has been done, namely that of Franco *et al.* (2005), who employ observations from 20 GPS sites along a 400-km-long stretch of the Mexican subduction zone from 99°W to 95°W. From 2-D forward modelling of the velocities of five GPS sites that are located within the limits of our study area, Franco *et al.* estimate that locking along the subduction interface offshore from the eastern edge of our network (extending east of 96.5°W) is 90–100 per cent, but that the plate interface is fully unlocked (0 per cent locking) beneath our study area, at distances of 55 to 120 km from the trench.

Based on many more data from this same area, we find that the degree of locking offshore from the eastern end of our network is 40 per cent or less (Fig. 16c), much weaker than inferred by Franco *et al.* We also find that the interface beneath much of the study area is strongly coupled, including areas where Franco *et al.* suggest the interface is fully unlocked. We attribute these large differences to spatial aliasing in the results reported by Franco *et al.* due to their large interstation spacing within the study area. In particular, we find compelling evidence for large variations in the degree of locking over distances of only 20 km (Fig. 17), whereas the distances between the stations that are employed by Franco *et al.* to estimate the degree of locking in the study area are as large as 90 km.

5.3.2 Japan, Kamchatka and Costa Rica

The pattern of interseismic deformation along the plate interface beneath our study area differs significantly from the pattern of interseismic locking reported by Mazzotti *et al.* (2000) for the subduction interface beneath much of Japan. Mazzotti *et al.* find that the numerous station velocities from the Japanese continuous GPS network are fit well by a model in which the subduction interface is fully and uniformly locked, in stark contrast with the heterogeneous pattern of coseismic rupture that is defined by previous earthquakes beneath Japan. Mazzotti *et al.* propose that this apparent difference can be resolved if the elastic strain that appears to accumulate interseismically in an apparently homogeneous manner, is released heterogeneously in space and time by a combination of large shallow-thrust earthquakes, slow earthquakes, and aseismic slip. Our results suggest an alternative explanation, namely, that the Japanese GPS network lies too far from the Japan trench seismogenic zone to resolve strongly locked regions that define seismic asperities and the intervening weakly coupled zones that may accommodate plate convergence through stable sliding or infrequent transient slip.

Our results support the conclusions reached by Burgmann *et al.* (2005), who apply boundary element modelling to the velocities of ∼20 widely spaced GPS sites from Kamchatka to test a variety of models for interseismic strain accumulation along the Kamchatka subduction zone. Burgmann *et al.* find that their GPS data are the most consistent with a model in which the Kamchatka subduction interface consists of strongly locked asperities that are located near the cores of historic earthquake rupture zones. Based on their inability to fit their data with models in which strong interseismic locking is imposed across the full extent of historic earthquake rupture zones offshore from their GPS network, they propose that the strongly locked cores of the seismic asperities that are defined by the historic rupture zones are likely to be surrounded by conditionally stable areas that slip aseismically at reduced convergence rates during the interseismic period but rupture during large earthquakes. Similarly, modelling of our dense GPS velocity field indicates that the area of the strongest interseismic locking beneath Oaxaca coincides with the core of the 1978 earthquake rupture zone (Figs 14 and

17), and that the degree of locking decreases to significantly lower values towards and beyond the edges of the 1978 rupture zone.

Our results also agree with conclusions reached by Norabuena *et al.* (2004), who use interseismic GPS station velocities from the Nicoya peninsula of Costa Rica to estimate the distribution of interseismic locking along the Costa Rica segment of the Middle America trench. Norabuena *et al.* conclude that their observations are best explained by a model with small, strongly locked areas of the subduction interface that are separated by freely slipping regions. Future continuous and campaign measurements from the now-heavily instrumented Nicoya peninsula will constitute an important independent comparison to our own results, given the similarities of the deformation rates, trench-to-coast distances and imaging resolutions in these two areas.

5.4 Earthquake hazard along the Oaxaca segment

Our evidence for strong interseismic locking across the rupture zone of the 1978 earthquake clearly suggests that this region is a potential source of future large earthquakes (Fig. 17). From an analysis of seismological data, Zuniga & Wyss (2001) conclude that the Oaxaca subduction segment at 96.7°W is incapable of initiating a future large earthquake. In contrast, our analysis indicates that the most rapid strain accumulation in the study area is centred at a longitude of 96.7°W. We find, however, that the subduction interface west of ∼97.3°W is only weakly locked (Fig. 14b), coinciding with the location of the Oaxaca seismic gap described by Brudzinski *et al.* (2007). Our analysis thus suggests that it is more likely that a major earthquake will initiate near 96.7°W, where strain accumulates rapidly, than near ∼97.3°W, where strain accumulation rates are relatively slower.

Using our best-fitting model for intertransient locking (Fig. 16c), we estimate that elastic energy across the 1978 rupture zone has recharged at an annual rate of 1.6×10^{19} N m during the 30 yr since 1978. This rate of elastic energy recharge implies a recurrence interval of 40 yr if the 1978 earthquake ($M_W = 7.8$) was characteristic for this segment. If we instead assume that the characteristic earthquake is somewhat smaller ($M_W = 7.6$) or larger ($M_W = 8.0$), the implied recurrence intervals are 20 and 80 yr, respectively.

5.5 General implications and future work

Our results clearly suggest that significant variations occur in the degree of locking across a plate interface over distances of only tens of kilometres. If similar strong variations in interseismic locking are an important feature of other subduction zones, the pattern of these variations could be useful for estimating the likely sources of future large earthquakes and for determining barriers (weakly coupled zones) to the along-strike propagation of large ruptures. Unfortunately, achieving similarly detailed images of the pattern of interseismic locking along many subduction zones and hence testing for spatial correlations between earthquake rupture locations and zones of strong interseismic coupling will be challenging, given the larger trench-to-coast distances that characterize many subduction zones and practical limitations in many areas on the locations and density of GPS stations.

Burgmann *et al.* (2005) describe and apply a forward modelling technique that enables tests for such correlations regardless of the number or spacing of the GPS sites along a particular subduction zone. Their technique determines whether acceptable fits to GPS site velocities can be achieved by models in which the pattern of interseismic locking is required to mimic the spatial pattern of coseismic rupture that is defined by previous large earthquakes from a given subduction interface. This technique therefore implicitly tests whether interseismic geodetic measurements of surface deformation and independent, seismologically-based constraints on the locations of previous earthquakes define a consistent pattern of seismic asperities along a subduction interface.

Much could be learned from dense campaign style GPS observations along the Mexican coastline, provided that they are corrected for the influence of the transient slip that frequently occurs in this region. Dozens of campaign sites have already been installed along the Mexican coast. If supplemented with additional stations to achieve the necessary station spacing, the resulting network would constitute a powerful array for imaging variations in the degree of locking along the underlying subduction interface and for determining whether such variations are correlated with other relevant observables such as the rupture areas of previous large earthquakes, microseismicity, Bouguer gravity or topography.

ACKNOWLEDGMENTS

Numerous people and institutions made this project possible. We thank CONACyT for generous scholarship support of FCM at the University of Wisconsin. Mexican funding for the field work and research was provided by CONACyT grant 33121-T, an UNAM-PAPIIT grant and grants IN121505 and IN123504 to ECC. National Science Foundation grants EAR-0104299 and EAR-05510887 and University of Wisconsin Vilas Foundation funds supported research by CDM. Field vehicles, equipment and personnel were supplied by the University of Guadalajara and UNAM. We thank INEGI for providing GPS observations from station OAXA to the University of Guadalajara. We thank Gerardo Cifuentes-Nava, Esteban Hernandez-Quintero, Alejandro Hurtado-Diaz, Neal Lord, Hector Medina and Daniel Solis Reyes for invaluable field support. We thank Zhen Liu and the anonymous reviewer for their suggestions and also thank Tim Masterlark and Kurt Feigl for advice about modelling the subduction process. Data from NSF-sponsored sites OXLP and OXMC and all the Oaxaca campaign sites are archived at UNAVCO.

REFERENCES

Altamimi, Z., Sillard, P. & Boucher, C., 2002. ITRF2000: a new release of the international terrestrial reference frame for earth science applications, *J. geophys. Res.,* **107,** 2214, doi:10.1029/2001JB000561.

Aster, R., Borchers, B. & Thurber, C., 2005. *Parameter Estimation and Inverse Problems,* Elsevier Academic Press.

Bassin, C., Laske, G. & Masters, G., 2000. The current limits of resolution for surface wave tomography in North America, *EOS, Trans. Am. geophys. Un.,* **81,** F897.

Brudzinski, M., Cabral-Cano, E., Correa-Mora, F., DeMets, C. & Márquez-Azúa, B., 2007. Slow slip transients along the Oaxaca subduction segment from 1993 to 2007, *Geophys. J. Int.,* **171**(2), doi:10.1111/j.1365–246X.2007.03542.x.

Burgmann, R., Kogan, M.K., Steblov, G.M., Hilley, G., Levin, V.E. & Apel, T., 2005. Interseismic coupling and asperity distribution along the Kamchatka subduction zone, *J. geophys. Res.,* **110,** doi:10.1029/2005JB003648.

Calais, E., Han, J.Y., DeMets, C. & Nocquet, J.M., 2006. Deformation of the North American plate interior from a decade of continuous GPS measurements, *J. geophys. Res.,* **111**(B06402), doi:10.1029/2005JB004253.

Currie, C.A., Hyndman, R.D., Wang, K. & Kostoglodov, V., 2002. Thermal models of the Mexico subduction zone: Implications

Q3

for the megathrust seismogenic zone, *J. geophys. Res.,* **107**(B12), doi:10.1029/2001JB000886.

DeMets, C., 2001. A new estimate for present-day Cocos–Caribbean plate motion: implications for slip along the Central American volcanic arc, *Geophys. Res. Lett.,* **28,** 4043–4046.

Douglas, A., Beavan, J., Wallace, L. & Townend, J., 2005. Slow slip on the northern Hikurangi subduction interface, New Zealand, *Geophys. Res. Lett.,* **32**(L16305), doi:10.1029/2005GL023607.

Dragert, H., Wang, K. & James, T.S., 2001. A silent slip event on the deeper Cascadia subduction interface, *Science,* **292,** 1525–1528.

Franco, S., Kostoglodov, V., Larson, K., Manea, V., Manea, M. & Santiago, J., 2005. Propagation of the 2001–2002 silent earthquake and interplate coupling in the Oaxaca subduction zone, Mexico, *Earth Planets Space,* **57,** 973–985.

Hansen, P., 1992. Analysis of discrete ill-posed problems by means of the L-curve, *SIAM Rev.,* **34**(4), 561–580.

Heflin, M. et al., 1992. Global geodesy using GPS without fiducial sites, *Geophys. Res. Lett.,* **19,** 131–134.

Iglesias, A., Singh, S., Lowry, A., Santoyo, M., Kostoglodov, V., Larson, K. & Franco-Sánchez, S., 2004. The silent earthquake of 2002 in the Guerrero seismic gap, Mexico (Mw = 7.6): inversion of slip on the plate interface and some implications, *Geofísica Internacional,* **43,** 309–317.

Kostoglodov, V., Singh, S., Santiago, J., Franco, S., Larson, K., Lowry, A. & Bilham, R., 2003. A large silent earthquake in the Guerrero seismic gap, Mexico, *Geophys. Res. Lett.,* **30,** 1807–1810.

Larson, K., Kostoglodov, V., Miyazaki, S. & Santiago, J., 2007. The 2006 aseismic slow slip event in Guerrero, Mexico: New results from GPS, *Geophys. Res. Lett.,* **34**(L13309), doi:10.1029/2007GL029912.

Lawson, C. & Hanson, R., 1974. *Solving Least Squares Problems,* Prentice-Hall, Englewood Cliffs, NJ.

Lay, T. & Schwartz, S., 2004. Comment on 'coupling semantics and science' in earthquake research, *EOS, Trans. Am. geophys. Un.,* **85,** 339–340.

Lowry, A., 2006. Resonant slow fault slip in subduction zones forced by climatic load stress., *Nature,* **442,** doi:10.1038/nature05055.

Lowry, A., Larson, K., Kostoglodov, V. & Bilham, R., 2001. Transient slip on the subduction interface in Guerrero, southern Mexico, *Geophys. Res. Lett.,* **28,** 3753–3756.

Mao, A., Harrison, C. & Dixon, T., 1999. Noise in GPS coordinate time series, *J. geophys. Res.,* **104,** 2797–2816.

Marone, C., 1998. Laboratory-derived friction laws and their application to seismic faulting, *Ann. Rev. Earth Planet. Sci.,* **26,** 643–696.

Marquez-Azua, B. & DeMets, C., 2003. Crustal velocity field of Mexico from continuous GPS measurements, 1993 to June, 2001: implications for the neotectonics of Mexico, *J. geophys. Res.,* **108**(B9), doi:10.1029/2002JB002241.

Masterlark, T., 2003. Finite element model predictions of static deformation from dislocation sources in a subduction zone: sensitivies to homogeneous, isotropic, Poisson-solid, and half-space assumptions, *J. geophys. Res.,* **108,** doi:10.1029/2002JB002296.

Masterlark, T., DeMets, C., Wang, H., Sanchez, O. & Stock, J., 2001. Homogeneous vs heterogeneous subduction zone models: coseismic and postseismic deformation, *Geophys. Res. Lett.,* **28,** 4047–4050.

Mazzotti, S., Le Pichon, X., Henry, P. & Miyazaki, S., 2000. Full interseismic locking of the Nankai and Japan-west Kurile subduction zones: an analysis of uniform elastic strain accumulation in Japan constrained by permanent GPS, *J. geophys. Res.,* **105,** 13 159–13 178.

McCaffrey, R., 1997. Statistical significance of the seismic coupling coefficient, *Bull. seism. Soc. Am.,* **87,** 1069–1073.

Norabuena, E. *et al.*, 2004. Geodetic and seismic constraints on some seismogenic zone processes in Costa Rica, *J. geophys. Res.,* **109**(B11403), doi:10.1029/2003BJ002931.

Obara, K., Hirose, H., Yamamizu, F. & Kasahara, K., 2004. Episodic slow slip events accompanied by non-volcanic tremors in southwest Japan subduction zone, *Geophys. Res. Lett.,* **31,** L23602, doi:10.1029/2004GL020848.

Ohta, Y., Freymueller, J., Hreinsdóttir, S. & Suito, H., 2006. A large slow slip event and the depth of the seismogenic zone in the south central Alaska subduction zone, *Earth planet. Sci. Lett.,* **247**(1–2), doi:10.1016/j.epsl.2006.05.013.

Ozawa, S., Murakami, M., Kaidzu, M., Tada, T., Sagiya, T., Hatanaka, Y., Yarai, H. & Nishimura, T., 2002. Detection and monitoring of ongoing aseismic slip in the Tokai region, central Japan, *Science,* **298,** 1009–1012.

Pacheco, J., Sykes, L. & Scholz, C., 1993. Nature of seismic coupling along simple plate boundaries of the subduction type, *J. geophys. Res.,* **98,** 14 133–14 159.

Pardo, M. & Suárez, G., 1995. Shape of the subducted Rivera and Cocos plates in southern Mexico: Seismic and tectonic implications, *J. geophys. Res.,* **100,** 12 357–12 374.

Reid, H., 1910. *The mechanics of the earthquake, The California earthquake of April 18, 1906,* Report of the State Earthquake Investigation Commission, 2.

Scholz, C., 1998. Earthquakes and friction laws, *Nature,* **391,** 37–42.

Singh, S., Havskov, J., McNally, K., Ponce, L., Hearn, T. & Vassiliou, M., 1980. The Oaxaca, Mexico, Earthquake of 29 November 1978: a preliminary report on aftershocks, *Science,* **207,** 1211–1213.

Smith, W. & Sandwell, D., 1997. Global sea floor topography from satellite altimetry and ship depth soundings, *Science,* **277,** 1956–1962.

Stark, P. & Parker, R., 1995. Bounded-variable least-squares: an algorithm and applications, *Comput. Stat.,* **10,** 129–141.

Stewart, G., Chael, E. & McNally, K., 1981. The November 29, 1978 Oaxaca, Mexico, earthquake: a large simple event, *J. geophys. Res.,* **86,** 5053–5060.

Suarez, G., Monfret, T., Wittlinger, G. & David, C., 1990. Geometry of subduction and depth of the seismogenic zone in the Guerrero gap, Mexico, *Nature,* **345,** 336–338.

Tajima, F. & McNally, K., 1983. Seismic rupture patterns in Oaxaca, Mexico, *J. geophys. Res.,* **88,** 4263–4276.

Thatcher, W. & Rundle, J., 1984. A viscoelastic coupling model for the cyclic deformation due to periodically repeated earthquakes at subduction zones, *J. geophys. Res.,* **89,** 7631–7640.

Turcotte, D. & Schubert, G., 1982. *Geodynamics: Applications of Continuum Physics to Geological Problems,* John Wiley, New York.

Wang, H., 2000. *Theory of Linear Poroelasticity with Applications to Geomechanics and Hydrogeology,* Princeton University Press.

Wang, K. & Dixon, T., 2004. 'Coupling' semantics and science in earthquake research, *EOS, Trans. Am. geophys. Un.,* **85**(18), 180–180.

Yoshioka, S., Mikumo, T., Kostoglodov, V., Larson, K., Lowry, A. & Singh, S., 2004. Interplate coupling and a recent aseismic slow slip event in the Guerrero seismic gap of the Mexican subduction zone, as deduced from GPS data inversion using a Bayesian information criterion, *Phys. Earth planet. Inter.,* **146,** 513–530.

Zhao, S., Muller, R., Takahashi, Y. & Kaneda, Y., 2004. 3-D finite-element modelling of deformation and stress associated with faulting: effect of inhomogeneous crustal structures, *Geophys. J. Int.,* **157,** 629–644.

Zumberge, J., Heflin, M., Jefferson, D., Watkins, M. & Webb, F., 1997. Precise point positioning for the efficient and robust analysis of GPS data from large networks, *J. geophys. Res.,* **102,** 5005–5017.

Zuniga, F. & Wyss, M., 2001. Most-and least-likely locations of large to great earthquakes along the Pacific coast of Mexico estimated from local recurrence times based on b-values, *Bull. seism. Soc. Am.,* **91,** 1717–1728.

Q4

Q5

Queries

Journal: GJI
Paper: gji3910

Dear Author

During the copy-editing of your paper, the following queries arose. Please respond to these by marking up your proofs with the necessary changes/additions. Please write your answers on the query sheet if there is insufficient space on the page proofs. Please write clearly and follow the conventions shown on the corrections sheet. If returning the proof by fax do not write too close to the paper's edge. Please remember that illegible mark-ups may delay publication.

Query Reference	Query	Remarks
Q1	Au: Refetrence Turcotte & Schubert (2002) is changed to Turcotte & Schubert (1982) to match the reference list. Please check.	
Q2	AU: Pleaase confirm the heading levels for 'Results'.	
Q3	Au: Please provide publisher location for Reference Aster *et al.* (2005).	
Q4	Au: Reference Sandwell & Smith() is changed to Smith & Sandwell (1997) to match the reference list. Please check.	
Q5	Au: Please provide publisher location for Reference Wang (2000).	

Key words

Authors are requested to choose key words from the list below to describe their work. The key words will be printed underneath the summary and are useful for readers and researchers. Key words should be separated by a semi-colon and listed in the order that they appear in this list. An article should contain no more than six key words.

GEOPHYSICAL METHODS
Time series analysis
Image processing
Neural networks, fuzzy logic
Numerical solutions
Fourier analysis
Wavelet transform
Instability analysis
Inverse theory
Numerical approximations and analysis
Persistence, memory, correlations, clustering
Probabilistic forecasting
Spatial analysis
Downhole methods
Tomography
Interferometry
Thermobarometry
Fractals and multifractals
Non-linear differential equations
Probability distributions
Self-organization

GEODESY and GRAVITY
Satellite geodesy
Reference systems
Sea level change
Space geodetic surveys
Seismic cycle
Transient deformation
Gravity anomalies and Earth structure
Geopotential theory
Time variable gravity
Earth rotation variations
Global change from geodesy
Lunar and planetary geodesy and gravity
Radar interferometry
Plate motions
Tides and planetary waves
Acoustic-gravity waves

GEOMAGNETISM and ELECTROMAGNETISM
Electrical properties
Electromagnetic theory
Magnetotelluric
Non-linear electromagnetics
Archaeomagnetism
Biogenic magnetic minerals
Dynamo: theories and simulations
Environmental magnetism
Geomagnetic excursions
Geomagnetic induction
Magnetic anomalies: modelling and interpretation
Magnetic and electrical properties
Magnetic fabrics and anisotropy
Magnetic mineralogy and petrology
Magnetostratigraphy
Palaeointensity
Palaeomagnetic secular variation
Palaeomagnetism applied to tectonics
Palaeomagnetism applied to geologic processes
Rapid time variations
Remagnetization
Reversals: process, timescale, magnetostratigraphy
Rock and mineral magnetism
Satellite magnetics
Marine magnetics and palaeomagnetics
Marine electromagnetics

GENERAL SUBJECTS
Geomorphology
Geomechanics
Glaciology
Hydrogeophysics
Ionosphere/atmosphere interactions
Ionosphere/magnetosphere interactions
Gas and hydrate systems
Ocean drilling
Hydrology
Ultra-high pressure metamorphism
Ultra-high temperature metamorphism
Tsunamis
Thermochronology
Heat flow
Hydrothermal systems
Mantle processes

COMPOSITION and PHYSICAL PROPERTIES
Microstructure
Permeability and porosity
Plasticity, diffusion, and creep
Composition of the core
Composition of the continental crust
Composition of the oceanic crust
Composition of the mantle
Composition of the planets
Creep and deformation
Defects
Elasticity and anelasticity
Equations of state
High-pressure behaviour
Fracture and flow
Friction
Fault zone rheology
Phase transitions

SEISMOLOGY
Controlled source seismology
Earthquake dynamics
Earthquake ground motions
Earthquake source observations
Seismic monitoring and test-ban treaty verification
Palaeoseismology
Earthquake interaction, forecasting, and prediction
Seismicity and tectonics
Body waves
Surface waves and free oscillations
Interface waves
Guided waves
Seismic anisotropy
Seismic attenuation
Site effects
Seismic tomography
Volcano seismology
Computational seismology
Theoretical seismology
Statistical seismology
Wave scattering and diffraction
Wave propagation
Acoustic properties
Early warning
Rheology and friction of fault zones

TECTONOPHYSICS
Planetary tectonics
Mid-ocean ridge processes
Transform faults
Subduction zone processes
Intra-plate processes
Volcanic arc processes
Back-arc basin processes
Cratons
Continental margins: convergent
Continental margins: divergent
Continental margins: transform
Continental neotectonics
Continental tectonics: compressional
Continental tectonics: extensional
Continental tectonics: strike-slip and transform
Sedimentary basin processes
Oceanic hotspots and intraplate volcanism
Oceanic plateaus and microcontinents
Oceanic transform and fracture zone processes
Submarine landslides
Submarine tectonics and volcanism
Tectonics and landscape evolution
Tectonics and climatic interactions
Dynamics and mechanics of faulting
Dynamics of lithosphere and mantle
Dynamics: convection currents, and mantle plumes
Dynamics: gravity and tectonics
Dynamics: seismotectonics
Heat generation and transport
Impact phenomena
Hotspots
Large igneous provinces
Lithospheric flexure

Obduction tectonics
Neotectonics
Diapir and diapirism
Dynamics and mechanics of faulting
Folds and folding
Fractures and faults
Kinematics of crustal and mantle deformation
High strain deformation zones
Crustal structure
Mechanics, theory, and modelling
Microstructures
Rheology: crust and lithosphere
Rheology: mantle
Rheology and friction of fault zones
Paleoseismology

PLANETS
Planetary interiors
Planetary volcanism

VOLCANOLOGY
Physics of magma and magma bodies
Magma chamber processes
Magma genesis and partial melting
Pluton emplacement
Effusive volcanism
Mud volcanism
Subaqueous volcanism
Explosive volcanism
Planetary volcanism
Volcaniclastic deposits
Volcano/climate interactions
Atmospheric effects (volcano)
Volcanic gases
Lava rheology and morphology
Magma migration and fragmentation
Eruption mechanisms and flow emplacement
Physics and chemistry of magma bodies
Calderas
Experimental volcanism
Tephrochronology
Remote sensing of volcanoes
Volcano monitoring
Volcanic hazards and risks
Volcano seismology

GEOGRAPHIC LOCATION
Africa
Antarctica
Arctic region
Asia
Atlantic Ocean
Australia
Europe
Indian Ocean
North America
Pacific Ocean
South America

MARKED PROOF

Please correct and return this set

Please use the proof correction marks shown below for all alterations and corrections. If you wish to return your proof by fax you should ensure that all amendments are written clearly in dark ink and are made well within the page margins.

Instruction to printer	*Textual mark*	*Marginal mark*
Leave unchanged	• • • under matter to remain	✓
Insert in text the matter indicated in the margin		New matter followed by or
Delete	/ through single character, rule or underline or ⊢⊣ through all characters to be deleted	 or 
Substitute character or substitute part of one or more word(s)	/ through letter or ⊢⊣ through characters	new character / or new characters /
Change to italics	— under matter to be changed	
Change to capitals	≡ under matter to be changed	≡
Change to small capitals	= under matter to be changed	=
Change to bold type	~ under matter to be changed	~
Change to bold italic	≈ under matter to be changed	
Change to lower case	Encircle matter to be changed	
Change italic to upright type	(As above)	
Change bold to non-bold type	(As above)	
Insert ‘superior’ character	/ through character or where required	 or  under character e.g. or 
Insert ‘inferior’ character	(As above)	 over character e.g.
Insert full stop	(As above)	⊙
Insert comma	(As above)	,
Insert single quotation marks	(As above)	 or  and/or  or
Insert double quotation marks	(As above)	 or and/or  or 
Insert hyphen	(As above)	⊢
Start new paragraph		
No new paragraph		
Transpose		
Close up	linking  characters	
Insert or substitute space between characters or words	/ through character or  where required	
Reduce space between characters or words	 between characters or words affected